



## Review

## Silicon-based materials as high capacity anodes for next generation lithium ion batteries

Bo Liang <sup>a,\*</sup>, Yanping Liu <sup>a</sup>, Yunhua Xu <sup>b</sup><sup>a</sup> Department of Material Forming and Control Engineering, School of Automobile and Mechanic Engineering, Changsha University of Science & Technology, Changsha 410076, PR China<sup>b</sup> Department of Chemical and Biomolecular Engineering, University of Maryland, College Park, MD 20742, USA

## H I G H L I G H T S

- The paper reviewed the merits of silicon-based anodes in lithium ion batteries.
- The mechanisms were discussed from in-situ TEM and first-principles simulation.
- The challenges faced in silicon-based anodes were analyzed and forecast.

## A R T I C L E I N F O

## Article history:

Received 2 October 2013

Received in revised form

30 April 2014

Accepted 21 May 2014

Available online 29 May 2014

## Keywords:

Lithium-ion batteries

Silicon

Anode

Composite

Nano-structure

## A B S T R A C T

Silicon (Si)-based materials have the highest capacity among the investigated anode materials and have been recognized as one of the most promising materials for lithium-ion batteries. However, it is still a significant challenge to obtain good performance for practical applications due to the huge volume change during the electrochemical process. To date, the most successful strategy is to introduce other components into Si to form composite or alloy materials. In this review, the recent progress in Si-based materials utilized in lithium-ion batteries is reviewed in terms of composite systems, nano-structure designs, material synthesis methods, and electrochemical performances. The merits and disadvantages of different Si-based materials, the understanding of the mechanisms behind the performance enhancement as well as the challenges faced in Si anodes are also discussed. We are trying to present a full scope of the Si-based materials, and help understand and design future structures of Si anodes in lithium-ion batteries.

© 2014 Elsevier B.V. All rights reserved.

## 1. Introduction

Among all investigated anode materials, silicon (Si) has a theoretical capacity of 3590 mAh g<sup>-1</sup> (almost ten times higher than that of graphite) based on the fully alloyed form of Li<sub>15</sub>Si<sub>4</sub> at room temperature (at high temperature Li<sub>22</sub>Si<sub>4</sub> can be reached, giving a capacity of 4200 mAh g<sup>-1</sup>), placing it on top of all other anode materials [1–3]. In addition, Si anodes show moderate working potential (~0.5 V vs. Li/Li<sup>+</sup>) [4], which, in contrast to graphite anodes (~0.05 V vs. Li), avoid the safety concern of lithium deposition upon cell overcharge as well as avert the energy penalty of battery cells assembled with the Li<sub>4</sub>Ti<sub>5</sub>O<sub>12</sub> anodes (1.5 V vs. Li/Li<sup>+</sup>) [5]. Fig. 1 showed a schematic of a lithium battery with a Si anode and a

lithium metal oxide (LiM<sub>x</sub>O<sub>y</sub>) intercalation cathode [3]. However, the large number of lithium ion insertion/extraction results in huge volume change (~370% assuming final alloy of Li<sub>15</sub>Si<sub>4</sub>), which leads to structural pulverization and electrical disconnection between the active materials and the current collector, and finally fast capacity fading [2]. To circumvent these problems, tremendous efforts have been attempted, including methods from physical to chemical, from inorganic to organic. Among them the most successful strategy is to incorporate other components into Si materials, such as polymers, carbon, and metals. Significant progress and promising results have been achieved based on these composites. The material designs and performance results will be summarized and discussed in the following sections.

Failure of the Si anodes is mainly caused by the large volume expansion/contraction during lithium insertion/extraction because the intermetallics of Li/Si have much greater molar volume than the nanostructure Si phase, as shown in Fig. 2 [6]. Large stresses

\* Corresponding author.

E-mail addresses: [liangbo26@126.com](mailto:liangbo26@126.com), [lbcut@126.com](mailto:lbcut@126.com) (B. Liang).

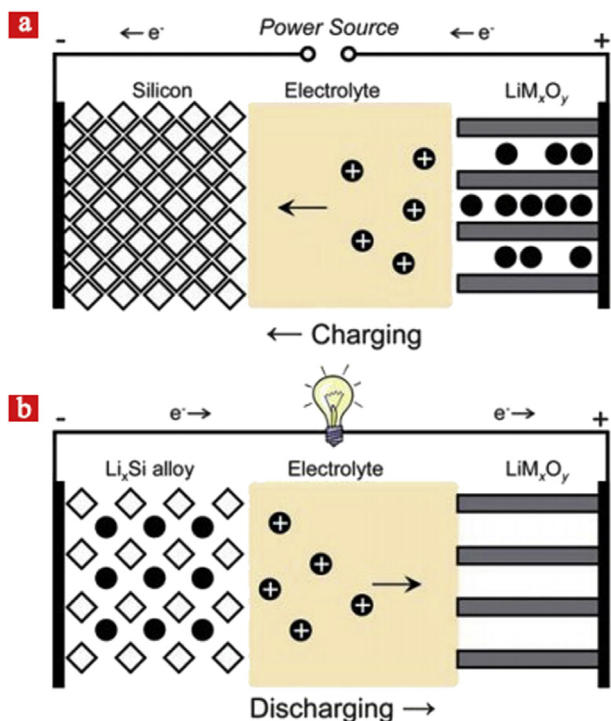


Fig. 1. Schematic of a lithium battery containing a Si anode and lithium metal oxide cathode during (a) charging and (b) discharging [3].

induced by the repetitive volume expansion and contraction can cause cracking and pulverization of the Si anodes, which leads to loss of electrical contact and eventual capacity fading [5,7–9] as shown in Fig. 3.

The behavior of lithiation-induced deformation and stress has been extensively studied in recent years. On the basis of theoretical calculation, several groups have investigated the lithium-insertion-induced swelling and stress and proposed or predicted the results in mechanical failure. For instance, Christensen and Newman calculated swelling and stress [10,11], Sastry and co-workers simulated the stress generation during lithiation under galvanostatic control [12], Cheng and coworkers calculated the strain energy under both potentiostatic and galvanostatic operations in spherical particles [13,14]. Lithiation-induced stress in Si has also been calculated [15,16]. Several recent papers have reported lithiation-induced fracture by applying electrochemical mechanics [17–19].

The large volume changes also cause significant challenges on the morphology and integrity of the entire electrodes. The drastic electrode morphology change can influence the integrity of the electrodes and further result in the capacity fading. The electrode

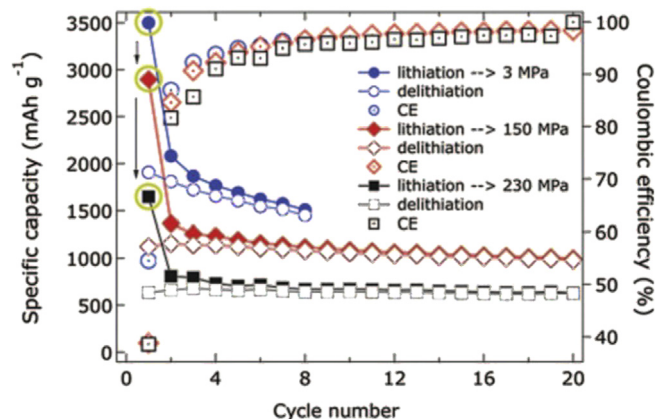


Fig. 3. Electrochemical performance and CE of solid-state nano-Si composite anodes cycled at a rate of C/20 under compressive pressures of 3 (blue), 150 (red) and 230 (black) MPa [9]. (For interpretation of the references to color in this figure legend, the reader is referred to the web version of this article.)

cracking and peeling-off have been observed by several research groups. Kim et al. investigated the variations in volume and density as a function of Li content [20]. They found that when the Li content was sufficiently high, alloying between Li and silicon was energetically favorable as evidenced by the negative mixing enthalpy; the alloy was most stable around 70 atom% Li in the crystalline phase and  $70 \pm 5$  atom% Li in the amorphous phase. Many other researchers also studied the volume expansion and received similar results [21–23]. The previous studies have shown that the large deformation of Si electrodes during electrochemical process could be alleviated by plastic flow [24]. The electrode morphology and integrity are especially relevant to the geometries of the nano-structured electrodes. Motivated by this phenomenon, Zhao et al. elucidated the plastic deformation in lithiated Si under uniaxial tension [23]. The microscopic mechanism of large plastic deformation is attributed to continuous lithium-assisted breaking and reforming of Si–Si bonds and the creation of nano-pores.

Solid-electrolyte interphase (SEI) film that resulted from the decomposition of electrolytes is another important factor in the battery performance, which leads to irreversible capacity loss. The formation of this passivating SEI film on the Si surface has been confirmed by high resolution transmission electron microscopy (HRTEM), Fourier Transform infrared spectroscopy (FTIR), and X-ray photoelectron spectroscopy (XPS) [25–27]. The SEI stability at the interface between Si and the liquid electrolyte is a critical factor in cycle life and coulombic efficiency. For example, Arie et al. investigated the electrochemical performance of phosphorus- and boron-doped nanostructure Si thin-film anodes [28]. They found that the doped Si showed much better cycling stability and higher capacity than the un-doped Si films, which is attributed to the formation of stable SEI layer on the surface of the doped electrodes.

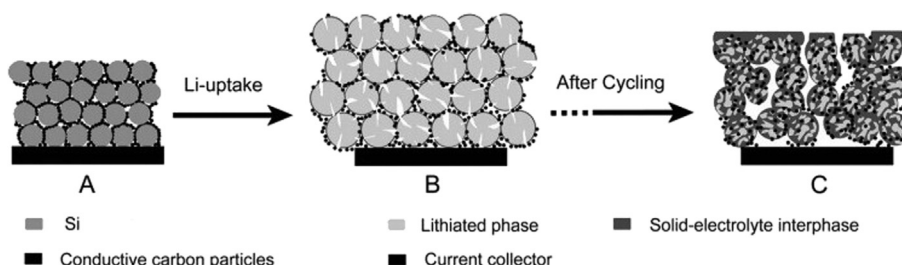


Fig. 2. Structure demolition of Si anode during lithium insertion [6].

On the contrary, the un-doped Si electrode showed high electrode polarization and poor cycling performance because of an unstable surface layer formed on the electrode surface.

In addition, the large volume change cracks the SEI films and makes Si expose to electrolytes, and thus keep the SEI films growing. As a result, active Si particles would be isolated by the electric-insulated SEI films and lose electrochemical activity, i.e. capacity fading.

## 2. Nanostructured silicon anodes

Here four generation nanostructures, namely hollow nanospheres, nanotubes, nanowire arrays, and porous structures was gone through. These nanostructures can effectively withstand the stress induced by heterogeneous changes in the volume of Si anodes without fracturing or improving the electrochemical properties of Si electrodes.

The action mechanism in hollow nanospheres is actually the same as that in nanotubes. During lithiation, the thin layers of the active materials thicken or expand inwards without structural fracture. During delithiation, the thickness of the lithiated layers and the morphology of the entire nanostructures can almost recover.

The electrochemical characteristics of hollow Si tubes have been shown to exhibit good performances [29–31]. Song et al. [29] developed a group IVA based nanotube heterostructure array, consisting of a high-capacity Si inner layer and a highly conductive Ge outer layer, to yield both favorable mechanics and kinetics in battery applications. This type of Si/Ge double-layered nanotube array electrode exhibits stable capacity retention (85% after 50 cycles) and doubled capacity at a 3 C rate. These results stem from reduced maximum hoop strain in the nanotubes, supported by theoretical mechanics modeling, and lowered activation energy barrier for Li diffusion. Park et al. fabricated novel Si nanotubes by reductive decomposition of a Si precursor in the alumina template and etching [31]. The use of Si nanotubes increased the surface area accessible to the electrolyte, allowing lithium ions to intercalate from both the interior and the exterior of the nanotubes. The nanotube electrodes have ultrahigh reversible charge capacities of 3200 mAh g<sup>-1</sup> with capacity retention of 89% after 200 cycles at a rate of 1 C in practical Li-ion cells with improved rate stability. After that, Song et al. reported a Si nanotube, consisting of arrays of sealed, tubular geometries capable of accommodating large volume changes associated with lithiation [30]. High initial coulombic efficiencies (~85%) and stable capacity retention (80% after 50 cycles) were obtained. Wen et al. described a promising strategy for large-scale fabrication of Si nanotubes prepared directly from Silica nanotubes [33]. The Si nanotubes showed significantly improved

rate capability and long-term cycling performance compared with commercial Si meshes, a capacity of ~1000 mAh g<sup>-1</sup> was retained after 90 cycles at a rate of 0.5 C. For hollow nanospheres, Cui and co-workers synthesized interconnected hollow Si nanospheres with an inner radius of about 175 nm and a layer thickness of about 25 nm, exhibiting a high initial discharge capacity of 2725 mAh g<sup>-1</sup> when used as anode materials in LIBs [34]. The discharge capacity only degraded by 8% per 100 cycles for 700 total cycles. The shell of the hollow spheres can also consist of irregularly arranged subunits (such as nanosheets, nanorods, and nanotubes) instead of one integral layer.

Si nanowires (SiNWs) have recently attracted intense attention for application as lithium-ion battery anodes [26,35–51] for the following attributes: (1) SiNWs can be directly connected to the current collector without additional binders or conducting additives; (2) SiNWs can offer direct one-dimensional electronic pathways for rapid charge transport; (3) SiNWs can provide rapid charge/discharge rates due to high surface-to-volume ratio; and (4) SiNWs with small diameters can accommodate large volume changes stemming from the alloying reaction and can prevent fragmentation.

Cui and coworkers designed high performance Si nanostructure anodes to fulfill the requirements of electric vehicles. In 2008, they reported a novel anodes made of vapor–liquid–solid (VLS) SiNWs, which was able to accommodate large strain caused by lithium ion insertion and extraction, as schematically shown in Fig. 4(a), (b) [35]. The SiNWs anode achieved a charging capacity of 4277 mAh g<sup>-1</sup> during the first charging operation and maintained a discharge capacity close to 75% of the maximum value during subsequent cycling (Fig. 4(c)). In another interesting work, Kumta and co-workers fabricated crystalline–amorphous core–shell SiNW-based anodes [35]. The core–shell SiNW anodes exhibited a high charge storage capacity three times that of carbon with 90% capacity retention over 100 cycles, and an excellent electrochemical performance.

After the pioneering work on SiNWs, numerous studies have been focused on nanowire-based electrodes to further improve the electrochemical performance of the SiNWs-based electrodes. Cui and coworkers also observed the SiNWs before and after lithiation and discovered their impacts on volume expansion [42,47,52–55]. In order to meet the significant quantities needed for commercial LIB applications, Aaron et al. demonstrated the creation of a SiNW nonwoven fabric and showed the specific capacity of 800 mAh g<sup>-1</sup> for a standalone anode material without the need of additional conductive fillers (activated carbon) or polymeric binders [48].

Several other approaches have been used to grow SiNWs. For example, Yang and coworker synthesized SiNWs on stainless steel foil by the Cu-catalyzed chemical vapor deposition (CVD) method,

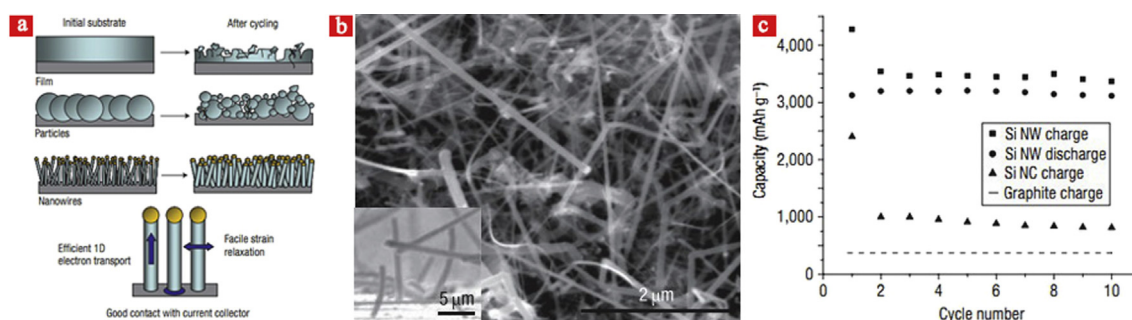


**Fig. 4.** Testing of Si nanowires as the battery anode. (a) Concept schematic of Si nanowire electrode assembled on the current collector; (b) scanning electron microscopy (SEM) image of Si nanowires that comprise the device anode; (c) capacity versus cycle number for various electrode configurations. The Si nanowires show stable capacity (~3500 mAh g<sup>-1</sup>) without any degradation with increase in the number of cycles [35].



showing a high coulombic efficiency of 89% at first cycle with a high specific capacity of over  $2000 \text{ mAh g}^{-1}$  in several dozens of cycles [56]. They confirmed that the introduction of vinylene carbonate (VC) additives into electrolytes greatly improved the cycle performance and rate capability of the SiNWs and showed a slow capacity degradation of 0.25% per cycle during 100 cycles test. The choices of catalyst affect the irreversible capacity loss for the anode. Emma et al. designed Sn catalyzed SiNWs using a high boiling point solvent-vapor-growth (SVG) system as a low cost approach to realize high density NW growth [57]. The SiNWs remained excellent capacities of  $1078 \text{ mAh g}^{-1}$  after 50 charge/discharge cycles.

Concurrently, Peng and coworkers demonstrated aligned metal-catalyzed electroless etching (MCEE) SiNWs as scalable anode materials for lithium-ion batteries [37]. In contrast to the VLS SiNWs [1], the MCEE SiNWs inherit the electrical characteristics of the original Si and thus no additional doping is needed. Moreover, the rough surfaces make MCEE SiNWs more promising for lithium-ion battery anode applications. The MCEE SiNWs showed a discharge capacity of nearly  $0.5 \text{ mAh cm}^{-2}$  and a longer cycling stability than bulk Si. The surface roughness of MCEE SiNWs increased after cycling due to the large volume change. Chakrapani et al. evaluated the performance of SiNW electrodes in ionic liquid (IL) and organic electrolyte [58], which showed good performance with charge and discharge capacities of 2014 and  $1836 \text{ mAh g}^{-1}$ . However, the electrode showed capacity fade of 20–30% both in IL and organic electrolyte after 50 cycles.

The good capacity retention of thin-film anodes was attributed to the strong adhesion of active material to the conductive support. Thin-film anodes can be prepared by magnetron sputtering [59–61] or physical vapor deposition [62–64]. The performance of thin-film anodes depends strongly on the deposition rate, deposition temperature, substrate-surface roughness, film thickness and post annealing treatment [65–67]. Takamura et al. reported that an amorphous Si thin film deposited 50 nm thick on a Ni foil exhibited a high specific capacity of over  $2000 \text{ mAh g}^{-1}$  and superior cyclability of over 1000 cycles at a charge rate of 12 C [62,68]. However, the cycle life was dramatically reduced when the film thickness was increased (200 cycles for 0.5–1  $\mu\text{m}$  films and 50 cycles for 1.8  $\mu\text{m}$  films) [67]. The poor performance of thicker films (>1  $\mu\text{m}$ ) compared to thinner films was due to the increased Li diffusion length, higher electrical resistance and larger internal stress of Li insertion/extraction [69,70].

Later, Pure Si thin flakes (Si Leaf Powder® (Si-LP)) of different thicknesses were prepared and used as negative electrode materials [71]. High reversible capacity ( $2200\text{--}2500 \text{ mAh g}^{-1}$ ) and good capacity retention were obtained for 50–200 nm Si-LPs. For the thinner flakes, agglomeration and large cracks were confirmed on the composite electrodes, but no pulverization of the flakes was observed. These data suggested that Li atoms diffused easily within the thinner Si-LPs and the uniformity of Li distribution suppressed the localized physical stress that caused by alloying and de-alloying.

Park et al. fabricated amorphous Si thin-films with a thickness of 1.5  $\mu\text{m}$  and 3  $\mu\text{m}$  by pulsed laser deposition, and found that the capacity of the former was superior to that of the latter [72]. Both films showed good cyclic performances without any abrupt fading in capacity up to 70 cycles. They attributed the good cyclic performance to strong adhesion behavior of the Si thin film and to the high density of the thin films. Paul et al. synthesized nano-structured Si thin films with varied oxygen content by evaporating Si in a water ambient using reactive ballistic deposition at glancing angles [73]. The incorporated oxygen concentration was controlled by varying the partial pressure of water during the deposition. The combination of homogeneous oxygen incorporation during the synthesis of the films and surface oxidation by low-temperature

annealing in air provides the best electrode stability. A high capacity ( $2200 \text{ mAh g}^{-1}$ ) was realized with virtually no capacity fade for the first 120 cycles and slight capacity fade ( $\sim 0.15\%$  per cycle) in cycles 150–300. Baggetto et al. [74] investigated the interaction between Si thin film electrodes and various electrolytes (liquid electrolyte:  $\text{LiClO}_4$  in propylene carbonate (PC),  $\text{LiPF}_6$  in ethylene carbonate (EC)/diethyl carbonate (DEC); solid electrolyte: lithium phosphorus oxynitride (LiPON),  $\text{Li}_3\text{PO}_4$ ). For liquid electrolytes, it was found that the SEI formation depended on the type of electrolyte used. For solid electrolytes, the deposition of a LiPON electrolyte layer rendered the activation of the interface a more complicated process compared to that of pure  $\text{Li}_3\text{PO}_4$ . An interlayer material due to partial intermixing was observed after depositing LiPON onto Si. Recently, some studies on patterned Si thin-film

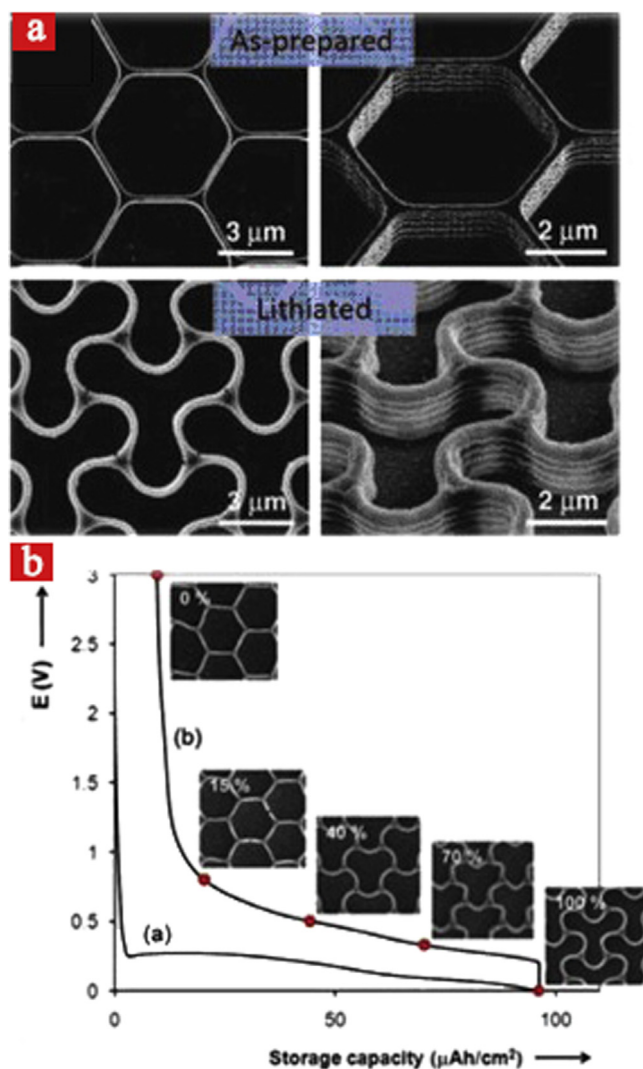


Fig. 5. (a) SEM image of the as-prepared and fully lithiated Si honeycomb. (b) Morphological change of the Si honeycomb structure during delithiation [76].

revealed interesting results and unique scientific insights [75–77]. Xiao et al. prepared patterned Si thin films on a Cu substrate by electron beam evaporation using three kinds of mesh masks [75]. Those Si patterns below 7–10  $\mu\text{m}$  remained adhered to the Cu substrate during cycling, leading to much better cycling stability and capacity retention than did patterns of other sizes. The

gaps between Si patterns allow stress relaxation and support better cycling stability relative to a continuous film. Baggetto et al. fabricated a honeycomb-structured Si film on planar TiN-covered Si substrate by photoetching [76]. After lithiation, the honeycombs became highly curved (Fig. 5(a)). The thickness, length and height of the curved wall all increased compared with the starting material. Fig. 5(b) illustrated the morphological changes during delithiation. Interestingly, the highly curved structure gradually converted back to its original configuration, and the hexagonal honeycombs were recovered finally, exhibiting only slight deformation. A patterned Si electrode to alleviate the cracking and reduce the side reactions was also reported by He and coworkers [77].

Although a quite number of Si nanostructures have been reported as anodes in lithium-ion batteries, nanostructure Si materials show fast capacity fading, which hinders the practical applications. Besides nanostructure Si, another structural design for solving the problem related to the volume change is the construction of composites, which consists of Si active materials and other components. The composites act as a buffer to alleviate the stress and accommodate the volume change led by lithium insertion/extraction. By using composites/alloys, the electrode integrity and the electronic contact between the active particles and conductive phase can be maintained [4,78]. A variety of composites with active/inactive materials and nanostructures have been designed and reported in the latest few years.

### 3. Silicon/carbon composites

#### 3.1. Silicon/amorphous carbon composites

Carbon coatings on Si electrodes have been reported to modify the SEI morphology and exhibited smooth surfaces with limited pore structure [79,80], compared to the visibly cracked and porous morphology seen in nanostructure Si electrodes [81]. Recently, nanocomposites with a nanocrystalline Si powder coated with a thin layer of amorphous carbon has led to moderate success of sustaining reversible capacities on the order of 700 mAh g<sup>-1</sup> at ~0.25 C in the electrochemical potential window of 0.02–1.2 V [82,83]. Carbon-coated Si particles have also been shown to achieve capacities as high as 1000 mAh g<sup>-1</sup> when charging and discharging at a constant current of ~0.3 mA mg<sup>-1</sup> [84]. Wilson et al. firstly obtained nanodispersed Si in carbon using CVD and received a reversible capacity of roughly 500 mAh g<sup>-1</sup> [34]. Similarly, Ng et al. synthesized a spheroidal carbon-coated Si nanocomposite anode, and an initial lithiation capacity of 2600 mAh g<sup>-1</sup> and a delithiation capacity of 1857 mAh g<sup>-1</sup> for the active materials (44% Si + 56% C) was obtained by using a nonrestricted cycling procedure [85].

Some studies were reported that nano-sized Si particles in composites tend to aggregate during charge/discharge cycles, and this size increase results in poor Li insertion/extraction kinetics [86,87]. Carbon-coated Si particles with an average size of 10 nm had a capacity over 3000 mAh g<sup>-1</sup> with an efficiency of 98% [87]. In order to prevent aggregation during the cycling, Kwon et al. reported the synthesis of Si quantum dots coated with amorphous carbon [88]. The new structures gained a first charge capacity of 1257 mAh g<sup>-1</sup> with a coulombic efficiency of 71%. The uniform distribution of Si quantum dots along with the carbon coating prevented aggregation during the cycling.

Huang et al. prepared coin cells using carbon-coated MCEE SiNWs as composite anodes [38]. Compared to simple SiNWs anode, the carbon-coated SiNWs composite anode exhibited an excellent first discharge capacity of 3344 mAh g<sup>-1</sup> with a coulombic efficiency of 84% and significantly enhanced cycling performance. TEM analysis showed most of the SiNWs remained continuous after

40 cycles with a few SiNWs breaking into particles due to non-uniform volume changes among nanowires. The performance improvement is ascribed to the carbon coating that facilitates electronic contact and conduction.

A hierarchical bottom-up self-assembly technique consisting of dendritic carbon structures coated with Si nanoparticles (SiNPs) has recently attracted attention [89]. A reversible charge (deintercalation) capacity of about 1950 mAh g<sup>-1</sup> was reached at a rate of 0.5 C. The specific capacity of the SiNPs alone was estimated to be 3670 mAh g<sup>-1</sup>, which is close to the theoretical value. The dendrite structure of carbon helped to provide efficient electron conduction by acting like a conducting backbone. It also provided the appropriate porosity required for the SiNPs to undergo volumetric expansion. Carbon inverse-opals coated with amorphous Si was synthesized via templating with ordered colloidal spheres and subsequent Si deposition. Its capacity was above 2100 mAh g<sup>-1</sup> after 145 cycles, whereas the capacity of a Si inverse-opal coated with amorphous carbon (Si/C inverse-opal) was completely lost by the 11th cycle [90].

Hu et al. reported a Si@SiO<sub>x</sub>/C nanocomposite in which pre-formed SiNPs were coated with carbon by hydrothermal carbonization of glucose [91]. The nanocomposite showed remarkably improved lithium-storage performance in terms of high reversible lithium-storage capacity (1100 mAh g<sup>-1</sup>) and high rate capability. However, the electrode was much less stable without the additive. Considering the construction of Si-based composites with hollow structures is another effective approach to improve the electrochemical performance, Cho and coworkers synthesized three-dimensional porous Si with an excellent capacity of 2800 mAh g<sup>-1</sup> at a rate of 1 C [92]. Park et al. reported SiNPs trapped in an ordered mesoporous carbon composite by a one-step self-assembly with solvent evaporation using a triblock copolymer Pluronic F127 and a resorcinol-formaldehyde polymer as the templating agent and carbon precursor respectively [93]. Such a one-pot synthesis of Si/ordered mesoporous carbon nanocomposite is suitable for large-scale synthesis. The composite showed a high reversible capacity above 700 mAh g<sup>-1</sup> during 50 cycles at 2 A g<sup>-1</sup>.

Deng et al. reported a tubular configuration made from naturally rolled-up C/Si/C trilayer nanomembranes, which exhibits a highly reversible capacity of approximately 2000 mAh g<sup>-1</sup> at 50 mA g<sup>-1</sup>, and approximately 100% capacity retention at 500 mA g<sup>-1</sup> after 300 cycles, as shown in Fig. 6 [94]. The naturally strain-released nanomembranes could enhance the capability to prevent stress cracking during the electrochemical cycles, and the tubular structures could facilitate fast ion diffusion and electron transport. The sandwich-structured C/Si/C composites, with moderate kinetic properties toward Li<sup>+</sup> ion and electron transport, are of the highest quality. The excellent cycling performance is related to the thin-film effect combined with carbon coating, which play a structural buffering role in minimizing the mechanical stress induced by the volume change of Si. The energy reduction in C/Si/C trilayer nanomembranes after rolling up into multi-winding microtubes results in a significantly reduced intrinsic strain, which can improve capacity and cycling performance. This synthetic process could be compatible with existing industrial sputtering deposition processes as well as roll-to-roll thin-film fabrication technology.

#### 3.2. Silicon/graphene composites

Graphene is an attractive option to improve the performance of the battery by enhancing the overall charge transportation mechanism [95]. The synthesis of Si/graphene composite is presented by a sonochemical method and then magnesiothermic reduction process [96]. Silica particles were firstly synthesized and deposited on the surface of graphene oxide (SiO<sub>2</sub>-GO) by ultrasonic waves,

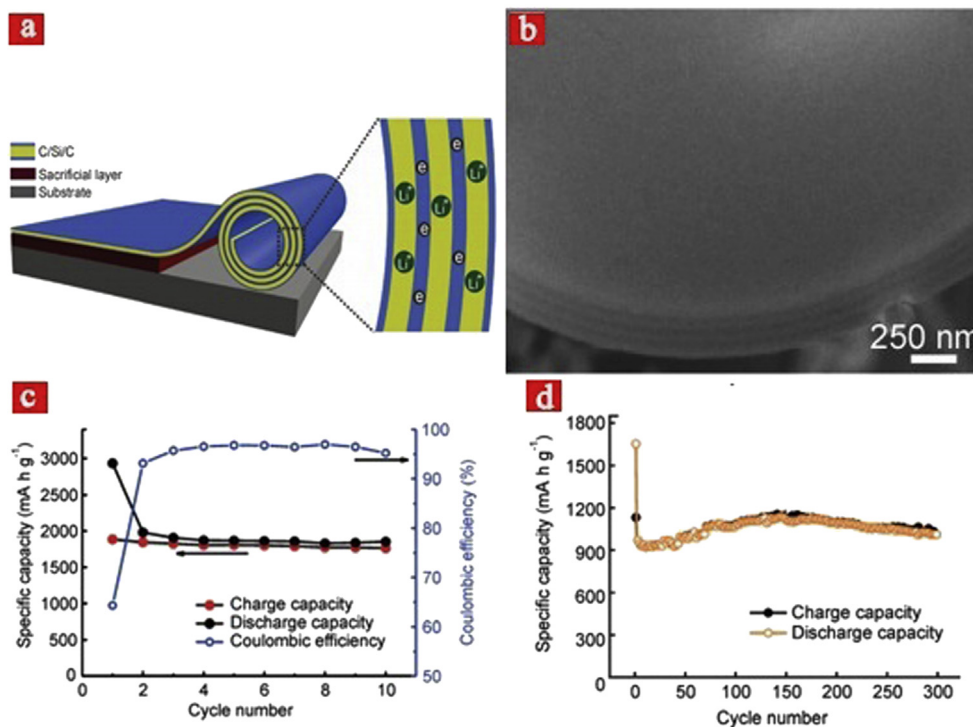


**Fig. 6.** (a) Fabrication of naturally rolled-up C/Si/C multilayer microtubes. (b) A cross-section of a single tube that prepared by focused ion beam (FIB) cutting, where tightly wrapped windings are visible; cycling performance showing the charge/discharge capacities of the as-prepared multilayer microtubes at current densities of approximately 50 mA g<sup>-1</sup>; (c) and 500 mA g<sup>-1</sup>; (d) from 0.05 V to 1.5 V versus Li/Li<sup>+</sup>, the capacity was calculated based on the total mass of the C/Si/C microtubes [94].

subsequent low-temperature magnesiothermic reduction transformed SiO<sub>2</sub> to SiNPs in-situ on graphene sheets. With the optimized ratio of 1:1, SiNPs on graphene sheets was obtained with the average particle size of 30 nm. The resultant Si-graphene with 78 wt% Si inside delivered a reversible capacity of 1100 mAh g<sup>-1</sup>, with very little fading when the charge rates change from 100 mA g<sup>-1</sup> to 2000 mA g<sup>-1</sup> and then back to 100 mA g<sup>-1</sup>. Similarly, a facile CVD method to prepare Si/carbon/graphite microspheres (Si/C/GM) composite anode by growing Si/C microrods on the surface of commercial GMs was reported [97]. The Si/C/GM composites with an urchin-like morphology are composed of Si particles, amorphous carbon, and graphite. The composite displayed the best anode properties with a specific capacity of 562 mAh g<sup>-1</sup> at a current density of 50 mA g<sup>-1</sup>, much higher than that of GMs (361 mAh g<sup>-1</sup>), and a good cycling performance (a reversible capacity of 590.5 mAh g<sup>-1</sup> after 50 cycles). The improved electrochemical performance is attributed to the incorporation of Si, together with the formation of a Si/C microrod network, which

connects the GMs and buffers the volume change of Si during lithium ion insertion/extraction. Very recently, Ren et al. introduced a chemical vapor deposition process to deposit crystalline Si particles onto graphene sheets by using a liquid chlorosilane as Si source [98]. The Si/graphene composite exhibits high utilization of Si in charge/discharge processes. The capacity retention of 90% after 500 full cycles and an average coulombic efficiency in excess of 99.5% are achieved in half cells. Zhou et al. presented a double protection strategy by fabricating graphene/carbon-coated SiNP hybrids to improve the electrochemical performance of Si in Li storage [99]. The graphene/carbon-coated SiNP hybrids exhibited outstanding reversible capacity of 902 mAh g<sup>-1</sup> after 100 cycles at 300 mA g<sup>-1</sup>. This work suggested a strategy to improve the electrochemical performance of Li-ion batteries by using graphene as supporting sheets for loading of active materials and carbon as the covering layers.

A unique graphene bonded and encapsulated Si anode using a one-step scalable aerosol spray method was researched (Fig. 7)

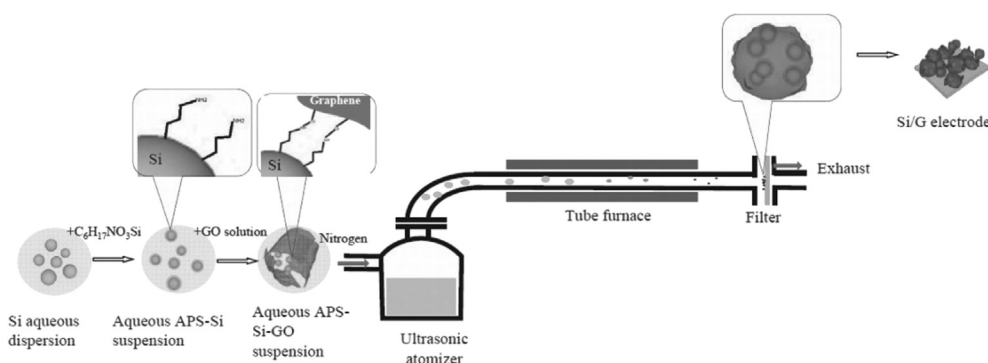


**Fig. 7.** Schematic procedure for the synthesis of graphene bonded and encapsulated nano-Si composite [100].



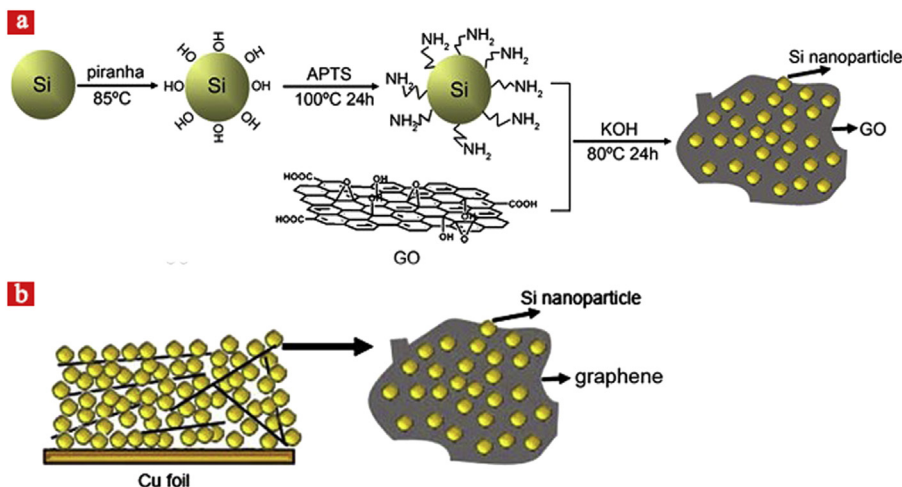


Fig. 8. (a) Scheme of fabricating Si-GO hybrid and (b) Si-graphene anode [34].

[100]. The functionalized Si sealed by graphene delivered a specific charge capacity of  $2250 \text{ mAh g}^{-1}$  at 0.1 C and retained 85% of its initial capacity even after 120 charge/discharge cycles. The open-ended graphene shell with defects allowed fast electrochemical lithiation/delithiation, good electronic conductivity for SiNPs and prevented them from aggregating during charge/discharge cycles. The space inside the graphene shell accompanied by its strong mechanical strength can effectively accommodate the volume expansion of Si upon lithiation. The homogeneous distribution of monolayer SiNPs were firmly anchored to graphene oxides (GOs) by covalent immobilization [34] (Fig. 8). The super high surface area

of graphenes produced a high stable cycle performance when the hybrid was used as anode material for lithium ion batteries. The capacity of the Si/graphene hybrid anode at the 50th cycle still retained  $1203 \text{ mAh g}^{-1}$ , which was 92.7% of the 1st cycle.

Lee et al. fabricated well-dispersed SiNPs supported by a 3D network of graphene sheets [101]. Intimate contact between nanoparticles and graphene sheets was essential for improved electrochemical performance. The Si/graphene composites exhibited high lithium ion storage capacity and cycling stability ( $>1500 \text{ mAh g}^{-1}$  after 200 cycles). Luo et al. developed a one-step aerosol assisted capillary assembly technique to create crumpled

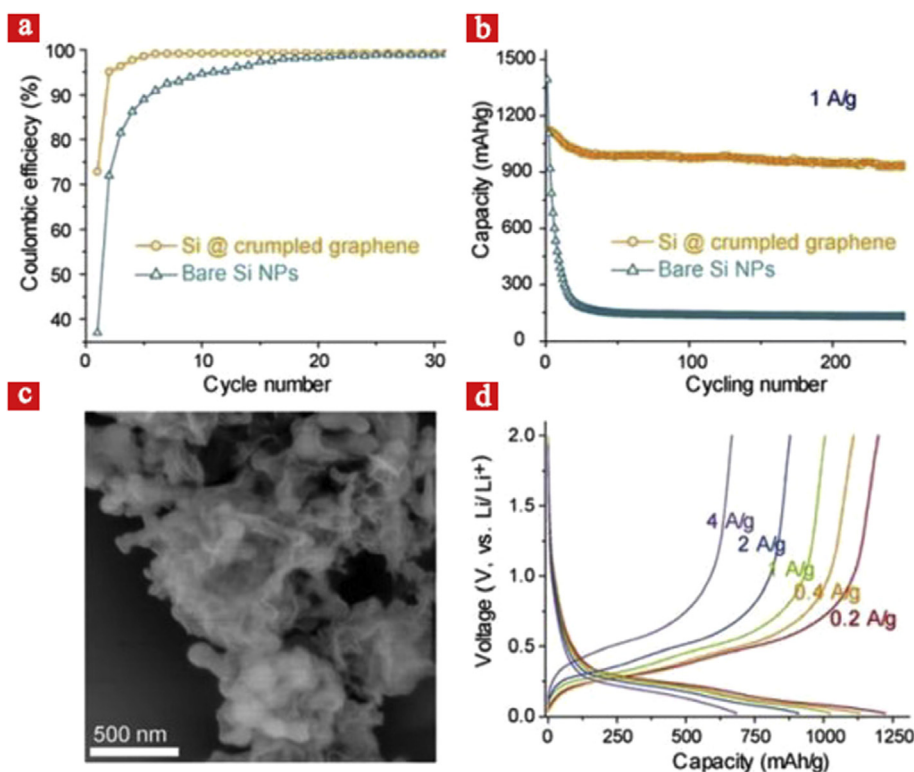
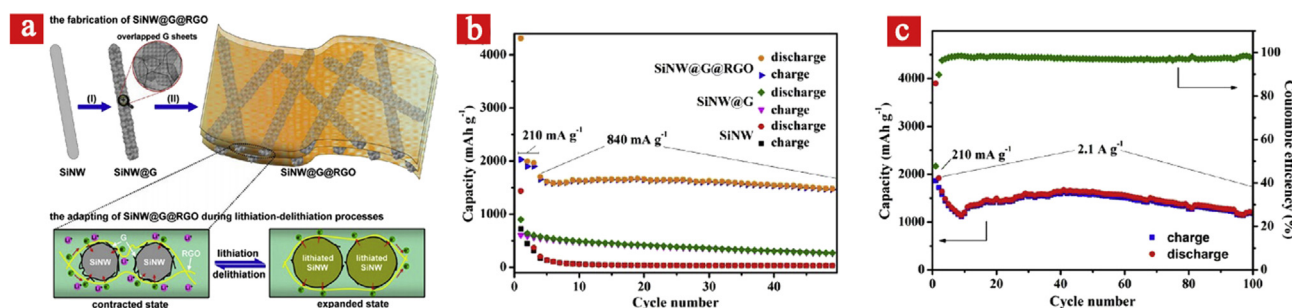


Fig. 9. Electrochemical performance of the capsules (Si@crumpled graphene). (a) Coulombic efficiency; (b) charge/discharge cycling test of the composite capsules in comparison to the unwrapped SiNPs at a constant current density of  $1 \text{ A g}^{-1}$ ; (c) SEM image of the capsules after 250 cycles showed that SiNPs were still encapsulated in the crumpled graphene; (d) galvanostatic charge/discharge profiles of the composite capsules electrode at various current densities ranging from 0.2 to  $4 \text{ A g}^{-1}$  [102].



**Fig. 10.** (a) Schematic of the fabrication (upper panel) and adapting (lower panel) of SiNW@graphene@RGO. The fabrication process mainly includes (I) CVD growth of overlapped graphene sheets on as-synthesized SiNWs to form SiNW@graphene nanocables, and (II) vacuum filtration of an aqueous SiNW@graphene-GO dispersion followed by thermal reduction. The resulting SiNW@graphene@RGO can transform between an expanded state and a contracted state during lithiation/delithiation cycles, thus enabling the stabilization of the Si material; (b) comparison of capacity retention of different electrodes. All electrodes were cycled at the charge/discharge rate of 210 mA g<sup>-1</sup> for the first three cycles and then 840 mA g<sup>-1</sup> for the subsequent cycles; (c) capacity and Coulombic efficiency of the SiNW@graphene@RGO cycled at the designated rate (210 mA g<sup>-1</sup> for the initial cycle and then 2.1 A g<sup>-1</sup>) for 100 cycles [105].

capsules of graphene-wrapped SiNPs [102]. As shown in Fig. 9, the composite delivered about 1200 mAh g<sup>-1</sup> at a low current density of 200 mA g<sup>-1</sup>. When the current density was increased 20 times from 0.2 to 4 A g<sup>-1</sup>, a capacity of 600 mAh g<sup>-1</sup> still remained.

Wang et al. reported that graphene nanosheets (GNSs) significantly improved the lithium storage capacity of porous single crystalline SiNWs [45]. Graphene acts as a conductive additive and the nanosheets cover larger areas of the nanowires, providing greater areas for charge transfer. The interleaved networks of GNSs should produce pathways for transport of electrons and lithium ions, improving both the electrical conductivity as well as the lithium ion diffusion rate of the electrode. The Si/graphene composites showed an initial charge capacity of 2347 mAh g<sup>-1</sup> with capacity retention of 87% after 20 cycles. Layer-by-layer alternation of GNSs coated Si nanocomposites with good cyclability and high capacities were also prepared by Sun et al. [103]. Zhu et al. prepared a well-defined core/shell self-assembly structure of SiNWs with spatially defined wrap of graphene [104]. The obtained GNS@SiNWs delivered a reversible capacity of 1648 mAh g<sup>-1</sup> with initial coulombic efficiency as high as 80%.

Wang and coworkers recently published a seminal paper to introduce a novel kind of self-supporting binder-free Si-based anode via the encapsulation of SiNWs with dual adaptable apparels (overlapped graphene sheaths and reduced graphene oxide (RGO) overcoats) (Fig. 10(a)) [105]. Within the novel architecture, the overlapped G sheets acted as adaptable but sealed sheaths, which could transform synergistically with the volume change of embedded SiNWs, prevent the direct contact of Si with the electrolyte, avoid the pore formation in Si, and thus secure the integrity of SiNWs during repeated cycling. Moreover, the RGO overcoats, as a mechanically robust and flexible matrix, accommodated the volume change of embedded SiNW@G nanocables, thus maintained the structural and electrical integrity of the electrode. They achieved a high reversible specific capacity of 1600 mAh g<sup>-1</sup> at 2.1 A g<sup>-1</sup>, 80% capacity retention after 100 cycles, and superior rate capability (500 mAh g<sup>-1</sup> at 8.4 A g<sup>-1</sup>) on the basis of the total electrode weight (Fig. 10(b)). The unique shape and structure of these nanocomposite not only allowed faster transport of the Li ions through the electrolyte and the electrode but also guaranteed faster intercalation reactions of the Li ions, thus resulting in a large specific capacity even when operated at high charge–discharge currents.

However, most of the Si/graphene composites resulted from freeze-drying [106], sonication followed by vacuum-filtration [101] or mechanical blending [107] did not exhibit acceptable performances, especially in cyclability. Composite anodes of SiNPs and RGO sheets with highly dispersed SiNPs were synthesized to investigate the performance-related improvements from particle

dispersion [108]. In spite of all the aforementioned advances in the field of composite anodes, the key issue of a weak structural interface between carbon and Si was not properly addressed. Si and carbon exhibited different volume changes associated with intercalation and de-intercalation of lithium ions. This in turn makes the composite vulnerable to rapid delamination, particularly at higher charge/discharge rates due to significant mismatch of the induced strains in Si and carbon.

### 3.3. Silicon/carbon fiber or nanotube composites

Among 1D carbonaceous material, CNTs are the most-popular additive for improving the electrochemical properties of Si-based materials. A homogeneous dispersion of SiNPs along thin CNTs allows optimizing of the electrochemical efficiency of Si [109]. The specific hierarchical hybrid nanostructure which deposited 10 nm SiNPs on thin CNTs of 5 nm in diameter delivered high reversible Li storage capacity of 3000 mAh g<sup>-1</sup> at 1.3 C. Li et al. prepared Si/carbon nanotube (CNT)/C composite for lithium-ion battery anode materials [110]. The carbon matrix accommodated the volume change of SiNPs and provided continuous pathways for efficient charge transport along the fiber axis. CNTs could improve the electronic conductivity and electrochemical performance of the composite anodes. Evanoff et al. reported a route to produce the large-scale fabrication of CNT fabric coated with Si for usage as an electrode for multifunctional Li-ion batteries [32]. The composite Si-CNT fabric showed ultimate tensile strengths (UTS) greater than 90 MPa after electrochemical cycling and the electrochemical performance of the electrodes demonstrated stability for more than 150 cycles. The same group explored ultra-thick electrodes composed of Si-coated carbon nanotube (CNT) arrays [111]. The electrode had average values of dealloying capacities of 3300 mAh g<sup>-1</sup> and 2000 mAh g<sup>-1</sup> at C/5 and C/2, respectively, and demonstrated good stability for over 250 cycles. Park and coworkers proposed the fabrication of self-supported multi-walled carbon nanotube (MWCNT)-embedded SiNP electrodes through CVD, with acetylene gas and a facile spin coating process using commercial Si nanopowders [112]. The void spaces between the MWCNTs were densely filled with a considerable amount of SiNPs with a diameter of ~50 nm. The MWCNT-embedded SiNP electrodes showed high specific capacity and superior capacity retention (2900 and 1510 mAh g<sup>-1</sup> after 10 and 100 cycles, respectively, at a current density of 840 mA g<sup>-1</sup>) as well as outstanding rate capability. These high electrochemical performances were ascribed to the roles of MWCNTs in terms of providing an efficient electron-transport path and alleviating volume change of SiNPs during Li-alloying/de-alloying process.



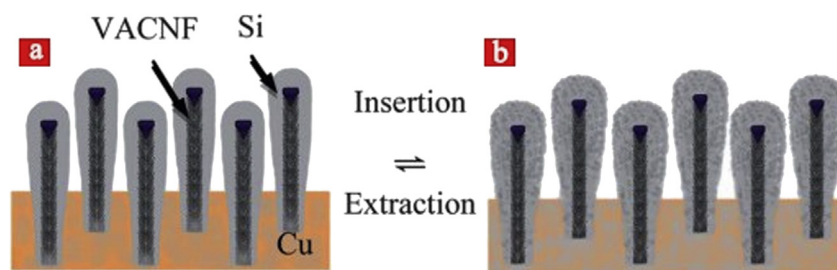


**Fig. 11.** Schematic illustration of the reversible structural changes of the coaxially coated Si on vertically aligned carbon nanofibers (VACNFs) in (a) extracted (discharged) and (b) inserted (charged) states during a half-cell test for Li-ion batteries [114].

Three-dimensional (3D) nano-architectures have attracted tremendous attention for applications in Li-ion batteries due to their unique structural advantages. Studies have further revealed that on anchoring SiNPs to carbon nanofibers (CNF), a significant specific capacity improvement achieved [113]. The carbonization process anchored the SiNPs induced a strong interaction between Si and carbon through thick amorphous Si oxide layer. The anode delivered a specific capacity of  $2500 \text{ mAh g}^{-1}$  at a current density of  $500 \text{ mA g}^{-1}$  and showed good capacity retention over 50 cycles. The polymer-like elasticity of the fibrous carbon matrix could further relieve the induced stress by accommodating Si volume expansion on Li insertion. Klankowski and coworkers reported a high-performance hybrid lithium-ion anode material using coaxially coated Si shells on vertically aligned carbon nanofiber (VACNF) cores (Fig. 11) [114]. The unique “cup-stacking” graphitic micro-structure made VACNFs a good lithium-ion intercalation medium and, more importantly, a robust bush-like conductive core to effectively connect high-capacity Si shells for lithium-ion battery. The vertical core-shell nanowires remained well separated from each other even after coating with bulk quantities of Si (equivalent to  $1.5 \mu\text{m}$  thick solid films). This open 3D nanostructured architecture allowed the Si shells to freely expand/contract in the radial direction during lithium-ion insertion/extraction. High-performance Li storage with a mass-specific capacity of  $3000\text{--}3650 \text{ mAh g}^{-1}$ , which was comparable to the maximum value of amorphous Si, was obtained even at the 1 C rate. About 89% of the capacity was retained after 100 charge–discharge cycles at the 1 C rate. The electrode material became even more stable after long cycling. High capacity near the theoretical limit was attained in over 120 charge/discharge cycles, showing the invariant lithium-ion storage capacity as the charge/discharge rate is increased by 20 times from 0.1 C to 2 C. Similar Si–C core–shell composites as lithium ion battery anodes have been reported by Cui and coworkers and other researchers as well [112,115–117]. Table 1 summarizes the most recent literature data on Si–C based electrodes for lithium-ion battery devices.

#### 4. Si/polymer composites

##### 4.1. Si/conducting polymer composites

To improve the cyclability of the Si-based anode, other components have been introduced to act as a buffer to accommodate the large volume change upon cycling. Conducting polymers (CPs) possess many advantages that make them suitable materials for lithium-ion battery, such as good conductivity, flexible mechanical property, and easy structure modification. The components of CPs not only function as a structural and physical buffer to minimize the mechanical stress, thus keep the particles together in powder-based anodes and make them adhere to the current collector, but also provide a conductive matrix to ensure a good kinetics.

Among the electronically-conducting polymers, polypyrrole (PPy) was the most used polymers as a positive electrode additive material in lithium ion batteries because it is easily doped with cations and anions to produce high conductivity and good stability in air [118,119]. Guo et al. reported a novel Si/PPy anode using high-energy mechanical milling [118]. It was found that dense agglomerates ( $0.3\text{--}3.0 \mu\text{m}$ ) of Si particles were connected by PPy. The Si/PPy anode with a 1:1 weight ratio of Si to PPy exhibited an initial discharge capacity of up to  $1800 \text{ mAh g}^{-1}$  and retained over 90% of the initial capacity after 10 cycles. The improved performance was attributed to the buffering and binding ability of the conductive PPy matrix. Better performance was obtained for anodes derived from PPy-coated Si particles prepared by in-situ polymerization [120] in which Si particles were coated with PPy via in-situ polymerizing pyrrole with  $\text{FeCl}_3$  (Fig. 12). A uniform thin layer of PPy (average thickness, about 2 nm) was formed on the surface of Si particles. The Li/PPy-coated Si electrode exhibited improved discharge capacities. Unfortunately, only short cycle life was reported on these composite anodes. The result indicated that PPy coating on the Si nanoparticles was not sustained during cycles, but may contribute in preventing the binding among the particles from losing and/or preventing cracked Si fragments from being extracted into the electrolyte.

PPy-coated Si nanofiber networks were prepared using a facile two-step approach: at first PPy nanofibers were synthesized by electropolymerization and then Si was deposited on the PPy fibers via a CVD procedure, as shown in Fig. 13(a). [121]. With this well-designed configuration, the PPy nanofibers conveniently maintain the structural integrity of the composite fibers and facilitate charge delivery and gathering, while the porosity of the electrode can adequately buffer the Si swelling during the lithiation process. The reversible capacity of the electrode remained as high as  $2800 \text{ mAh g}^{-1}$  after 100 cycles, corresponding to 91% of the first cycle (Fig. 13(b)). Good rate capability was also observed on the composite fibers. The well-preserved morphology of reticular nanofibers after repeated lithium insertion and extraction demonstrated the robust ability of the PPy nanofibers.

In order to increase electronic conductivity, Ag was introduced into the Si/PPy composites by chemical polymerization of pyrrole and reduction of  $\text{AgNO}_3$  [122]. Ag not only increased the conductivity but also provided strong mechanical property of the composites. For the optimal amount of Ag in the Si/PPy composites, the cycle stability and rate capability of the Si-PPy-Ag composites were greatly enhanced in comparison with the bare SiNPs. A high capacity of more than  $823 \text{ mAh g}^{-1}$  was retained after 100 cycles, showing its promising application as anode materials for lithium-ion batteries.

The effects of different microstructures of PPy, nano-wires and micro-particles, on the electrochemical performance were investigated [123]. In comparison with the bare Si particles, better performance was observed for the Si/PPy nano-wires that contain

**Table 1**  
Electrochemical performance of Si–C composite anodes for lithium-ion batteries.

Anode	Specific capacity (mAh g <sup>-1</sup> )	Cycling stability	Synthesis methods	References
Carbon-coated Si	1000	1000 mAh g <sup>-1</sup> after 57 cycles	Fluidized-bed type of chemical vapor deposition	[84]
Carbon-coated Si	2600	1489 mAh g <sup>-1</sup> after 20 cycles	Spray-pyrolysis technique	[85]
Si/ $\alpha$ -C	1257	Capacity retention after 30 cycles was 84%	Annealing at 700 or 900 °C	[88]
Si/dendritic C	3670	50 wt% of Si 1950 mAh g <sup>-1</sup> at C/20, volumetric capacity was determined to be 1270 mAh cm <sup>-3</sup> at C/20	Hierarchical bottom-up assembly technique	[89]
Si/C	2100	2100 mAh g <sup>-1</sup> after 145 cycles	Templating	[90]
Si@SiO <sub>x</sub> /C	1100	A current density of 150 mA g <sup>-1</sup>	Coated carbon by hydrothermal carbonization on glucose	[91]
Si/C	1275	Reversible capacity of 700 mAh g <sup>-1</sup> during 50 cycles at 2 A g <sup>-1</sup>	One-step self-assembly with solvent evaporation	[93]
C/Si/C film	2000	Approximately 100% capacity retention at 500 mAh g <sup>-1</sup> after 300 cycles	Naturally roll-up C/Si/C trilayer nanomembranes	[94]
C/SiNWS	3344	At a rate of 150 mA g <sup>-1</sup> between 2 and 0.02 V	metal catalytic etching of Si wafers and pyrolyzing of carbon aerogel	[38]
SiNW/GNSs	2347	2041 mAh g <sup>-1</sup> at the 20th cycle, 87% capacity retention after 20 cycles	Liquid-phase graphite exfoliation method and an electroless HF/AgNO <sub>3</sub> etching process	[45]
Si/graphene	1100	A reversible capacity of 1300 mAh g <sup>-1</sup> , little fading from 100 to 2000 mA g <sup>-1</sup> back to 100 mA g <sup>-1</sup>	Combination of sonochemistry and Mg-assisted reduction	[96]
Si/C/GMS	562	A reversible capacity of 590.5 mAh g <sup>-1</sup> after 50 cycles	Chemical vapor deposition	[97]
Si/graphene sheets	1365	553 mAh g <sup>-1</sup> retained after 500 cycles.	Chemical vapor deposition	[98]
Si/graphene	902	Remained 902 mAh g <sup>-1</sup> after 100 cycles at 300 mA g <sup>-1</sup>	Wrapped Si nanoparticles between graphene and amorphous carbon	[99]
APS–Si–graphene	2250	76% of initial capacity after 120 charge/discharge cycles at 1 C	Scalable aerosol spray method	[100]
Si/graphene	1500	1500 mAh g <sup>-1</sup> after 200 cycles	3D network of grapheme sheets	[101]
Si/graphene	1200	940 mAh g <sup>-1</sup> after 250 cycles	One-step capillary-driven assembly route in aerosol droplets.	[102]
SiNW/G/RGO	1600	500 mAh g <sup>-1</sup> at 8.4 A g <sup>-1</sup> , 80% capacity retention after 100 cycles	Chemical vapor deposition and thermal reduction	[105]
Si/CNT/C	1410	837 mAh g <sup>-1</sup> at the 30th cycle, the 57.6% capacity retention with 300 mA g <sup>-1</sup> at the 50 cycle	Electrospinning and carbonization	[110]
$\alpha$ -Si/C	3086	Capacity retention displaying ~0.03% fade in capacity up to 50 cycles and ~0.2% after 50 cycles	Radio frequency magnetron sputtering	[227]
Si/CNT	2000	~1000 mAh g <sup>-1</sup> at the 100th cycle	Two-step liquid injection chemical vapor deposition process	[228]
Si/CNF	4050	3890 mAh g <sup>-1</sup> after 100 cycles	A unique dual plasma deposition technique	[229]
Si/PCNF	2643	~1104 mAh g <sup>-1</sup> under 0.5 A g <sup>-1</sup> after 100 cycles, with a capacity retention of 69.1%	A single-nozzle electrospinning technique and subsequent calcination and HF etching process	[230]
Si/C-PDA	2691	1601 mAh g <sup>-1</sup> at the 50th cycle, 72.6% after 50 cycles	Conventional electrospinning and multiple depositions and annealing	[231]
Si film/CNT	2083	1711 mAh g <sup>-1</sup> after 50 cycles, with 82% capacity retention	Chemical vapor deposition of a-Si on CNT films or by CNT-SiNP compositing technique	[232]

10 wt% PPy, while no improvement for Si/PPy micro-particles was observed. The possible reason is that the vast network of PPy nanowires matrix can accommodate the huge volume change during the alloying/dealloying reactions.

Polyaniline (PANi), another conducting polymer, was also used in Si composite anodes. Cai et al. synthesized Si/PANi composites by chemically polymerizing aniline on Si nanoparticles [124]. The initial delithiation capacity was 1940 mAh g<sup>-1</sup> at 100 mA g<sup>-1</sup> and maintained a capacity of 1870 mAh g<sup>-1</sup> after 25 cycles with a capacity fading rate of 0.3% per cycle. PANi/Si composite materials prepared by dispersing Si-NPs in PANi have been used as the electrode material for supercapacitors [125]. The PANi/Si composite showed high power (220 W g<sup>-1</sup>) and energy-storage (30 Wh kg<sup>-1</sup>) capabilities as well as good device stability during 1000 charging/discharging cycles. However, the composites showed limited rate capability, especially at high charge and discharge current

densities, indicating that the conductivity of the composites should be further improved.

Very recently, Cui group reported a well-connected three dimensional network structure of a SiNPs/PANi composite. SiNPs were conformally coated by the conducting polymer using in-situ polymerizing with SiNPs dispersed in hydrogel. This hierarchical hydrogel framework has multiple advantages: continuous electrically conductive PANi network, binding between Si and polymer, and porous space for volume expansion of Si particles. With these features, excellent performance was demonstrated: a cycle life of 5000 cycles with over 90% capacity retention at current density of 6.0 A g<sup>-1</sup>.

Poly(3,4-ethylenedioxythiophene) (PEDOT), one of the most successful conducting polymers, has received great attention for applications in material sciences. PEDOT has high electrical conductivity in the p-doped state, fast electrochemical switching, and

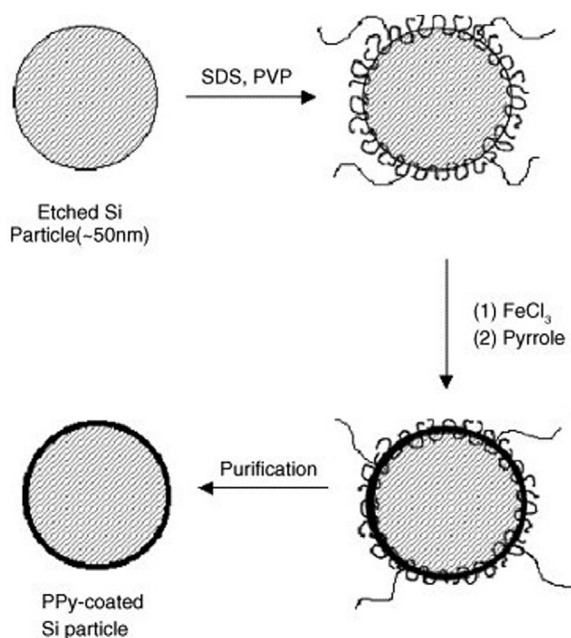


Fig. 12. Schematic representation for the preparation of PPy-coated Si particles [120].

good thermal and chemical stability. But it is soluble in common solvents, which makes it difficult to process in current fabrication technologies. Poly(styrenesulfonate) (PSS) is usually used as a charge-balancing dopant and dispersing agent during polymerization to form a stable aqueous suspension of PEDOT:PSS. PEDOT/PEDOT:PSS is attractive for use in lithium-ion batteries due to its polymer flexibility and high electric conductivity. It has been studied as cathode materials or additives of cathode materials in lithium-ion batteries [126–128]. Additionally, previous studies show that the heteroatom sulfur contained in each repeat unit of both PEDOT and PSS may improve the electrochemical performance when used in anode materials [129–132].

Zhang and co-workers reported a nano-Si/carbon composite with S-doped carbon matrix, which was prepared from an in-situ chemical polymerization of EDOT with nano-Si particles in a PSS aqueous solution and subsequent carbonization of Si/PEDOT:PSS [133]. A good cycling stability was obtained with capacity retention of  $768 \text{ mAh g}^{-1}$  and a columbic efficiency of 99.2% after 80 cycles.

Zhang and co-workers prepared Si/S-doped C composites by a magnesiothermic reduction reaction of mesoporous  $\text{SiO}_2$ , subsequently coated with sulfur-containing polymer (PEDOT) and post-carbonization [134]. The Si/S-doped C composite materials

exhibited a remarkably improved lithium storage performance, capacity retention, and rate capability. The Si/S-doped C composite displayed a first discharge capacity of  $1947 \text{ mAh g}^{-1}$  with first coulombic efficiency of 76.1% and cycling performance with a capacity of  $539 \text{ mAh g}^{-1}$  at the 100th cycle, which are much better than those of bare Si electrode.

Yao et al. coated the conductive polymer of PEDOT on Si nanowires (SiNWs) [135]. The PEDOT-coated Si-NWs demonstrated improved cycling stability, increasing the capacity retention after 100 charge/discharge cycles from 30% to 80% over bare SiNWs. The improvement in cycling stability was attributed to the conductive coating that maintained the mechanical integrity of the cycled Si material and preserved the electrical connections between SiNWs.

#### 4.2. Effects of polymer binders on Si anodes

Polymer binders are components used in preparation of electrodes to keep the integrity of the electrodes. Previous studies show that binders play a critical role in cell performance. A number of polymers have been investigated as binders in lithium-ion batteries.

Polyvinylidene fluoride (PVDF), one conventional binder, exhibits a good ductility and has been examined for Si anodes [136–139]. But it was not a good binder agent. The Si anodes using PVDF always suffered fast capacity fading [136,140]. In contrast, respectable Li-ion battery performance was obtained with poly (acrylic acid) (PAA), sodium carboxymethyl cellulose (CMC), and sodium alginate. They all have carboxylic functional groups and are soluble in water with environment-friendly characteristic. CMC, a bio-derived polymer, was used as a promising binder for Si electrodes [141–145]. Superior cycle stability, high capacity, and high energy and power density was demonstrated on a Si-NPs/CMC scaffold structure. At 1.5 C, the CMC scaffold-nano-Si electrode could provide discharge capacity of  $1800 \text{ mAh g}^{-1}$  (75% of the capacity at 0.05 C) [145].

Pure PAA, possessing certain mechanical properties comparable to those of CMC but containing a higher concentration of carboxylic functional groups, offer superior performance as a binder for Si anodes [146]. Komaba and coworkers reported PAA and its polymer salts [sodium polyacrylate (PANA)] led to graphite-Si electrodes with good reversibility [139,147–150]. The polyacrylates improved the binding ability (adhesion strength) of the composite electrode. The thin coating layer of polyacrylates uniformly covered the active materials and suppressed electrolyte decomposition as well as self-discharges.

Cross-linked PAA can be modulated by the addition of the polycarbodiimide (PCD) as a cross-linker [151]. The initial reversible capacity of Si/graphite composite electrodes was increased with

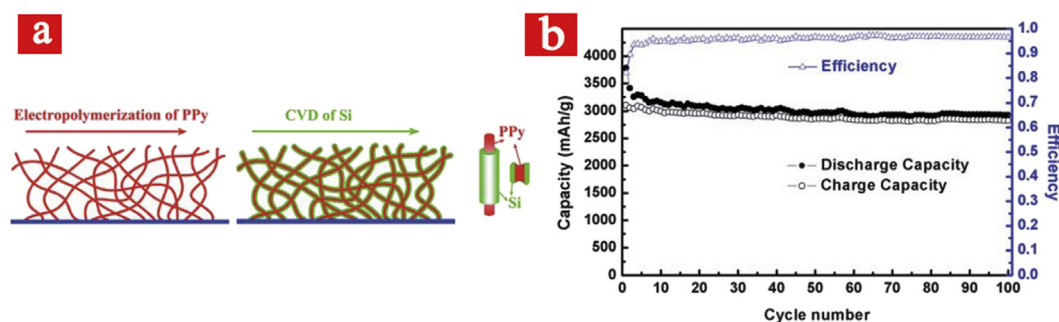
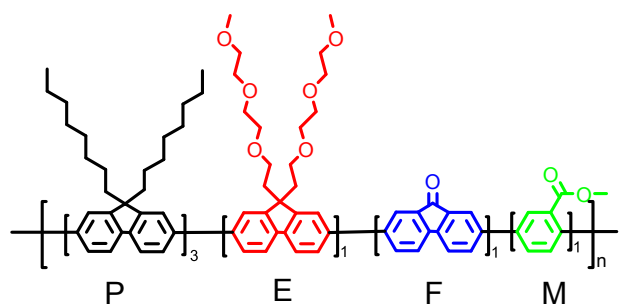


Fig. 13. (a) Schematic illustration of the synthesis procedure of 3D reticular PPy-Si core-shell nanocables. The PPy backbone network (red) is synthesized by electropolymerization, and Si (green) is deposited by CVD as the lithium storage host; (b) discharge/charge capacity and coulombic efficiency versus cycle number for the PPy-Si nanostructured electrode [121]. (For interpretation of the references to color in this figure legend, the reader is referred to the web version of this article.)







**Fig. 16.** The molecular structure of the functional groups incorporated in polymer binder, P: polyfluorene with octyl side chains; E: fluorene with triethyleneoxide monomethyl ether side chains; F: fluorenone; M: methyl benzoate ester [155].

conductivity and mechanical integrity during the battery operation, holding the promise of dual functionality of both binder and conductive additive. Liu et al. developed a new conductive binder to address the volume change problems in high capacity through a combination of advanced materials synthesis, spectroscopic analysis and theoretical simulations, as shown in Fig. 15 [154]. The integrated experimental and theoretical results showed that the developed polymer features improved electronic conductivity and robust mechanical binding forces, which simultaneously maintained electrical connectivity and accommodated the Si volume change. Composite electrodes based on Si particles and poly (9,9-dioctylfluorene-co-fluorenone-co-methylbenzoic acid (PFFOMB) binder, without any conductive additive, exhibited high capacity, long-term cycling, low over potential between charge and discharge, and good rate performance. The same group developed a multifunctionality binder polymer to maintain high electronic conductivity, mechanical adhesion, ductility, and electrolyte uptake

[155]. These critical properties were achieved by designing polymers with proper functional groups PEFM, as shown in Fig. 16. Cycling of Si particles with a full capacity of  $3750 \text{ mAh g}^{-1}$  was demonstrated from the multifunctionality conductive polymer binder. Table 2 summarized recent reports on Si/polymer based electrodes for lithium-ion battery devices.

## 5. Si-based alloys/composites

Si-germanium (Ge) alloys have been extensively studied for application in the semiconductor industry. Recently, Ge was studied as energy storage materials due to its high electronic conductivity, ionic diffusivity and capacity by several groups [156–160]. It has been found that Ge acts as a buffer against the volume change of the Si and contributes to the elevating lithium ion diffusion [161].  $\text{Si}_{0.41}\text{Ge}_{0.34}\text{Mo}_{0.25}$  nanocomposites with high energy density (1st charge,  $1193 \text{ mAh g}^{-1}$ ), long cycle ability ( $\sim 870 \text{ mAh g}^{-1}$  over 100 cycles), and high initial coulombic efficiency ( $\sim 96\%$ ) were prepared by Hwang et al. using a magnetron sputtering method [162]. Song developed a Si/Ge double-layered electrode based on nanotube heterostructure array, consisting of a high-capacity Si inner layer and a highly conductive Ge outer layer, to yield both favorable mechanics and kinetics in lithium ion battery applications [29]. The electrode exhibited improved electrochemical performances over the analogous homogeneous Si system, such as higher capacity retention after 50 cycles at a 3 C rate. These results stem from reduced maximum hoop strain in the nanotubes supported by theoretical mechanics modeling, and lowered activation energy barrier for Li diffusion. Hashimoto et al. prepared a  $\text{Li}_{4.4}\text{Si}_{(1-x)}\text{Ge}_x$  composite using ball milling process, which was applied as an active material in all-solid-state batteries [163]. Wang et al. investigated  $\text{Si}_{(1-x)}\text{Ge}_x$  that was sputtered onto a copper nanowire array and found that capacity retention varied with its composition, with

**Table 2**  
Electrochemical performance of Si/polymer composite anodes for lithium-ion batteries.

Anode	Specific capacity ( $\text{mAh g}^{-1}$ )	Cycling stability	Synthesis methods	Reference
Si/PPy	1800	Specific capacity 90% of the initial capacity after 10 cycles	High-energy mechanical milling	[118]
Si/PPy	—	568 $\text{mAh g}^{-1}$ capacity of the 50% Si/50% PPy composite electrode after 10 cycles.	Chemical polymerization	[119]
Si/PPy	2590	1000 $\text{mAh g}^{-1}$ discharge capacity in the 10th cycle	In-situ polymerization	[120]
Si/PPy	3076	$\sim 91\%$ reversible capacity remaining after 100 cycles	In-situ polymerization	[121]
Si/PPy/Ag	1816	823 $\text{mAh g}^{-1}$ after 100 cycles	Chemical polymerization method	[122]
Si/PANi	1940	1807 $\text{mAh g}^{-1}$ after 25 cycles with a capacity fading rate of 0.3% per cycle	Chemical polymerization process.	[124]
Si/PEDOT:PSS	936	768 $\text{mAh g}^{-1}$ after 80 cycles, with an initial capacity fade of 0.48% per cycle	In-situ chemical polymerization	[133]
Si/PEDOT:PSS	1947	539 $\text{mAh g}^{-1}$ after 100 cycles, a reversible capacity of $450 \text{ mAh g}^{-1}$ at a current rate of $6000 \text{ mA g}^{-1}$ .	Magnesiothermic reduction of mesoporous $\text{SiO}_2$ , coating with S-containing polymer (PEDOT), and post-carbonization	[134]
Si/Alginate	3040	1200 $\text{mAh g}^{-1}$ after 1300 cycles	A high-modulus natural polysaccharide extracted from brown algae.	[136]
Si/PCD	1000	Capacity retention 75% after 30 cycles	Cross-linked poly(acrylic acid) (PAA) with polycarbodiimide (PCD) utilized as a binder	[151]
Si/PFFOMB	2050	1400 $\text{mAh g}^{-1}$ ( $2100 \text{ mAh g}^{-1}$ for Si) after 650 cycles	Dispersing Si nanoparticle in the conductive polymer chlorobenzene solution	[154]
Si/PEFM	3650	The PEFM binder effectively maintained stable capacity over the 50-cycles	100% utilization of Si material embedded in the PEFM binder	[155]
SiNW/TMV1cys	3343	1656 $\text{mAh g}^{-1}$ at 4 C, 0.20% loss per cycle at 1 C	Metal coatings on patterned 3D TMV1cys templates used as a substrate	[180]

the most optimal composition of  $\text{Si}_{0.6}\text{Ge}_{0.4}$  [164]. In contrast with these deposition techniques, Mullins et al. synthesized nanostructured amorphous thin films by glancing angle deposition (GLAD) [165]. The electronic conductivity increases while the specific capacity decreases as germanium content increases. Additionally, the high-rate performance of the material increased substantially with increasing germanium content. However, the high cost and low abundance of germanium are hurdles to its generalization [166]. Very recently, Geaney et al. grew Si/Ge axial heterostructure nanowires with high yield using a versatile wet chemical approach [167]. Heterostructure nanowires growth was achieved using the vapor zone of a high boiling point solvent as a reaction medium with an evaporated tin layer as the catalyst. The precise tuning of the heterostructure nanowires interface would allow for exact determination and control of transport properties at the atomic level and greatly enhance their application in electronic devices.

Sakaguchi et al. [168] synthesized  $\text{TiO}_2/\text{Si}$  composites by sol–gel method and evaluated the electrochemical properties of the thick-film electrodes using the composites. The remarkably improved performance was obtained for the composite electrodes of  $\text{TiO}_2/\text{Si}$  (43/57 wt%): the discharge capacity of  $710 \text{ mAh g}^{-1}$  could be achieved at the 900th cycle.

Kim and coworkers synthesized nanocomposites of Si and titanium nitride (TiN) by using high-energy mechanical milling [169]. Si particles were homogeneously distributed inside the TiN matrix. The electrochemical activities of the obtained lithium ions nanocomposites were investigated, in which TiN provided structural stability. Zhou et al. synthesized a unique heteronanostructure that consists of two-dimensional  $\text{TiSi}_2$  nanonets (NNs) and particulate Si coating (Fig. 17(a)) [170]. The high conductivity and structural integrity of  $\text{TiSi}_2$  nanonets core were proved as great merits to permit reproducible lithium ions insertion and extraction into and from the Si coating. Nanoscale Si particles are attached to the NNs as the medium to react with lithium ions. This heteronanostructure was tested as the anode material for lithium ions storage. At a charge/discharge rate of  $8400 \text{ mA g}^{-1}$ , the electrode delivered specific capacities of over  $1000 \text{ mAh g}^{-1}$  and showed only an average of 0.1% capacity fade per cycle between the 20th and the 100th cycles (Fig. 17(b)). The good performance, high capacity, long capacity life, and fast charge/discharge rate made it one of the best anode materials that have been reported. The remarkable performance was attributed to its capability to preserve the crystalline of

the  $\text{TiSi}_2$  core during the charge/discharge process. It was also found that there was a large capacity fade in the first 10 cycles. The possible reason is that  $\text{TiSi}_2$  backbone alloyed with Li ions at a potential of 60 mV, which could destruct the backbone structure and result in the fast capacity loss. The cycling stability can be improved by applying a narrower charge/discharge voltage window to exclude the  $\text{TiSi}_2$  reaction. Mesoporous  $\text{TiO}_2$  has also been tested as a Li battery anode at high rates of 10 C and 20 C. However, the capacities were relatively low ( $\sim 140 \text{ mAh g}^{-1}$  and  $\sim 100 \text{ mAh g}^{-1}$  at the respective C-rates [171]). In addition, the preparation process of the above composite materials was too complex and unfavorable for its commercial application.

Park et al. reported a simple synthesis of  $\text{Ti}_x\text{Si}_y$  coated SiNPs via a silicothermic reduction process, in which Si acted as the reducing agent and titanium oxide as a source material of Ti [172]. The synthetic approach of  $\text{Ti}_x\text{Si}_y$ -coated SiNPs is briefly described in Fig. 18(a). The  $\text{Ti}_x\text{Si}_y$ -coated Si electrodes showed significantly improved high thermal stability compared to bare Si electrodes. When a cell was heated above a certain temperature, exothermic reactions between the electrodes and the electrolyte took place and led to an increase of the internal cell temperature. If the generated heat is greater than the energy that can be dissipated, the cell temperature will increase rapidly, accelerating chemical reactions, eventually resulting in the thermal runaway of batteries. As depicted in Fig. 18(b), the  $\text{Ti}_x\text{Si}_y$  coating layer can effectively mitigate various exothermic reactions caused by the thermal decomposition reactions of an electrolyte with lithiated Si at elevated temperatures. Thus, the titanium silicide enhanced the electrical conductivity of SiNPs and provided a highly stable solid electrolyte interface layer during the cycling. As a result, high reversible capacity ( $1470 \text{ mAh g}^{-1}$ ) and high rate capability ( $1150 \text{ mAh g}^{-1}$  at 20 C rate) were demonstrated (Fig. 18(c), (d)).

Ohara et al. reported a Si film deposited on a Nickel (Ni) substrate [64]. The cycle life was significantly improved because Ni develops a passivating layer that acted as an excellent binding agent between the substrate and the Si film, which is essentially due to the strong affinity of Si to oxygen. These cells showed capacities of as high as  $1700\text{--}2200 \text{ mAh g}^{-1}$  for 750 cycles at a 2 C charge/discharge rate. Later, nanocrystalline Si-embedded Ni–Ti composite anode materials were synthesized using a two-stage high-energy mechanical milling (HEMM) method by Soo et al. [173]. Cells with 10 h milled powders showed relatively low capacity fading, which was attributed to the nanocomposite structure

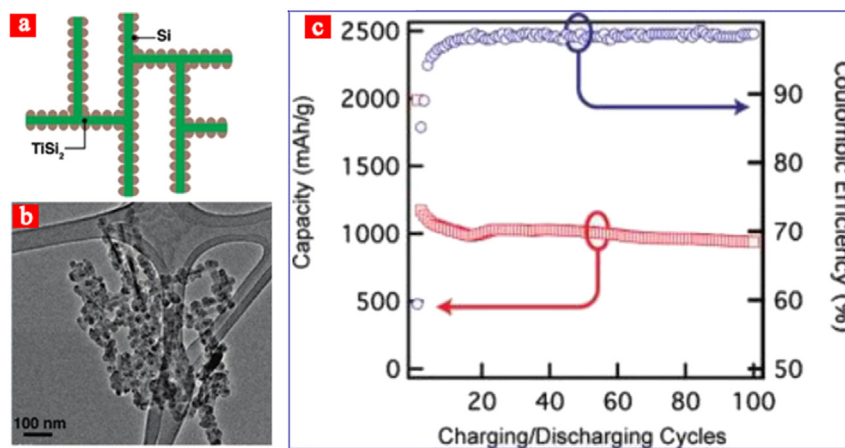


**Fig. 17.** (a) Schematic of the Si/ $\text{TiSi}_2$  heteronanostructure. SiNPs are deposited on highly conductive  $\text{TiSi}_2$  nanonets to act as the active component for Li storage; (b) a low-mag TEM picture manifests the particulate nature of the Si coating on  $\text{TiSi}_2$  nanonets; (c) charge capacity and coulombic efficiency of the Si/ $\text{TiSi}_2$  heteronanostructure with  $8400 \text{ mA g}^{-1}$  charge/discharge rate tested between 0.15 and 3.00 V [169].



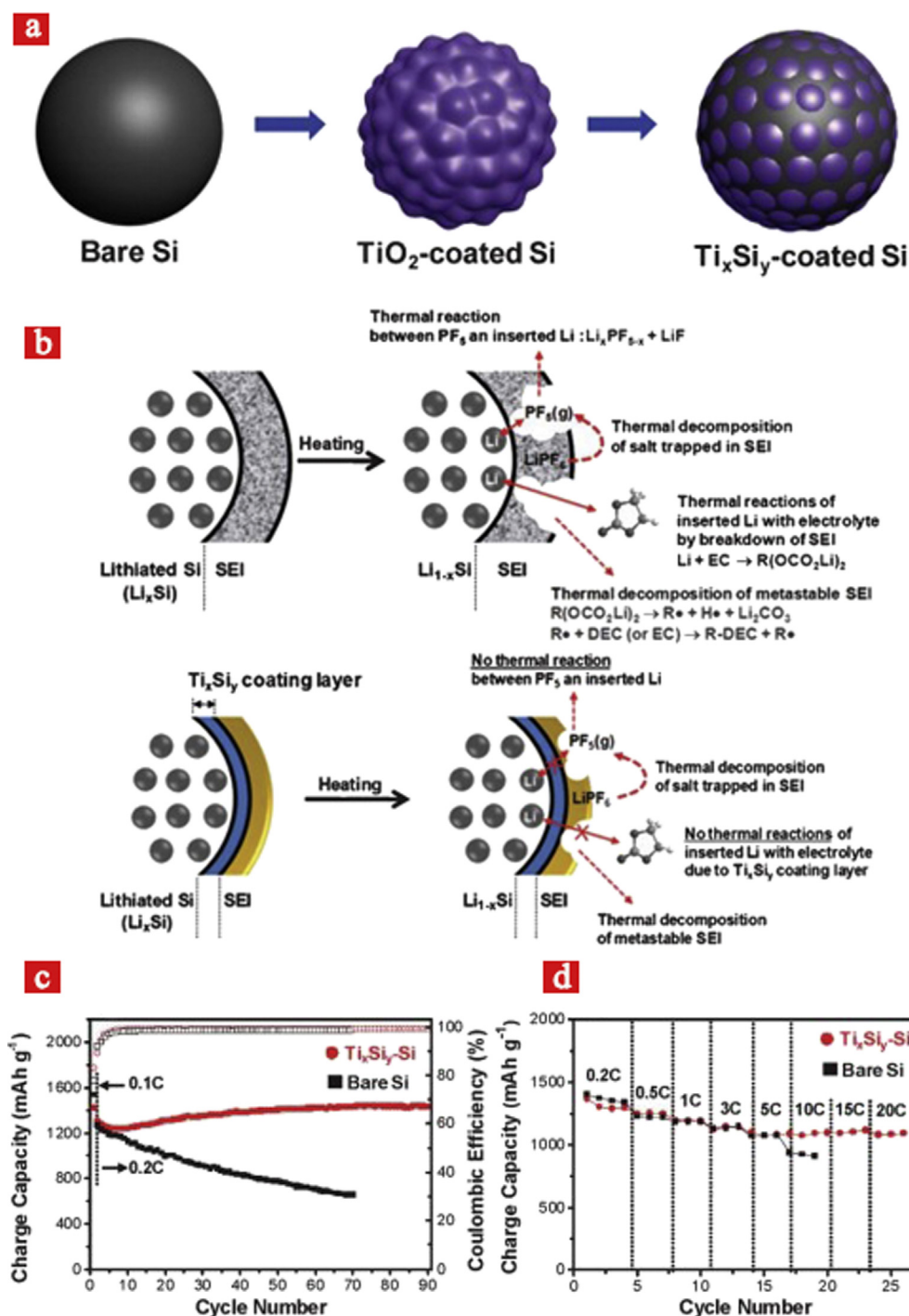


**Fig. 18.** (a) Schematic illustration preparing  $\text{Ti}_x\text{Si}_y$  layer on the surface of Si particles; (b) schematic illustration showing the thermal decomposition reactions of an electrolyte with lithiated Si at elevated temperatures; (c) cycling performances of both electrodes are obtained at 0.1 C (first cycle) and 0.2 C (from second cycle); (d) rate capabilities of  $\text{Ti}_x\text{Si}_y$ -coated Si (solid circle) and bare Si (solid square) were obtained at 0.2 C–20 C rates [172].

that comprised of Si nanocrystals embedded in the amorphous Ni–Ti matrix phase.

Sakaguchi et al. [174] coated Si particles with Ni, Ni–Sn, and Ni–P by using the electroless deposition (ELD) technique, and fabricated thick-film electrodes by the gas deposition (GD) method using the coated-Si particles. The electrode of Ni-coated Si had a discharge capacity of  $580 \text{ mAh g}^{-1}$  at the 1000th cycle. The electrode of Si coated with  $\text{Ni}_3\text{P}$  with a lower coating amount exhibited higher initial capacity and excellent cycling performance with a

capacity of  $750 \text{ mAh g}^{-1}$  at the 1000th cycle. The excellent performance in the case of the  $\text{Ni}_3\text{P}$  coating can be attributed to the smaller amount of coating, its high elastic modulus, and the moderate reactivity of  $\text{Ni}_3\text{P}$  with Li.

Zhang et al. reported the fabrication and characterization of a nanoscale Ni metal scaffold supported bicontinuous 3D Si anode [175]. This structure provided both conductivity pathway and mechanical support, which maintained a good electrical connectivity and stable structure during cycling. The initial capacity of the

bicontinuous Si anode was 3568 (Si basis) and 1450 mAh g<sup>-1</sup> (including the metal framework) at 0.05 C. 85% of the capacity remained after 100 cycles at 0.3 C. Although the 3D porous scaffold could eliminate the usage of the current collector foil and decrease the total mass of inactive parts, Ni is a relatively dense metal and additional research on lightweight electrochemically stable conductive 3D scaffolds may further advance this concept.

There is a growing interest in harnessing the viruses for use in energy-storage device [176,177]. The experiment revealed that the virus is electro-chemically inactive and stable. Different from previously reports on the synthesis of nanomaterials using biological templates where the active materials were mixed with binding and conductive agents and cast on current collectors, Wang et al. directly fabricated a Ni-core/Si-shell nanowire array electrode using a virus template [178]. They developed Tobacco mosaic virus (TMV) as a novel bioinorganic template that can be easily patterned on metal substrates to form nanoscaled 3D structures [179]. In this work, SiNW anodes were constructed by electrochemically depositing Si on a 3D current collector of self-assembled and Ni-coated TMV1cy array [180,181]. The virus-assembled nano-structures produced a 13–80 fold increase in reactive surface area. The nano-structured 3D Si anodes provided high capacities (3300 mAh g<sup>-1</sup>), good charge–discharge cycling stability (0.20% loss per cycle at 1 C), and excellent rate capabilities (46.4% at 4 C) [180]. They also constructed Si anodes using an electrochemical deposition method on the TMV1cys/Ni nanowire current collectors. The electrochemical deposited TMV1cys/Ni/Si structure provided

high capacity (2300 mAh g<sup>-1</sup>) as well as improved stability (>1200 mAh g<sup>-1</sup> at 173 cycles) with a high columbic efficiency (99.5%).

Copper (Cu) coating on Si has also been reported to enhance the electrical conductivity of Si anodes, which is due to the formation of a thin layer of Cu<sub>3</sub>Si alloy at the interface of Cu and Si [182]. Increased coulombic efficiency and cycling stability have been demonstrated on the Cu-coated Si anodes compared to carbon-coated Si electrodes [183,184]. Joyce et al. investigated the influence of copper coating as both a binder and conductive additive on the electrochemical performance of Si electrodes [185]. They found that copper coating layer formed a metallic net on Si and identified the existence and the electrochemically activity of the interfacial layer of silicides. A unique, scalable chemical approach for synthesizing copper-coated amorphous Si particles (Cu-coated a-Si:H) through a polyol reduction method was reported by Stevenson et al. [186]. The Cu-coated a-Si:H particles exhibited significantly enhanced lithium storage capacity over pristine a-Si:H particles in about sevenfold. They attributed the enhancement to the improved charge transfer kinetics by the copper coating. High charge storage capacity and improved cycling stability was observed.

Vlad et al. demonstrated an operational full cell 3.4 V lithium-polymer Si nanowire (LIPOSIL) battery which is mechanically flexible and scalable to large dimensions [187]. As shown in Fig. 19, an electroless growth protocol was developed to wrap the Si nanowires with a thin porous, electrically interconnected Cu layer. The conformal Cu-wrapped Si nanowires showed an improved

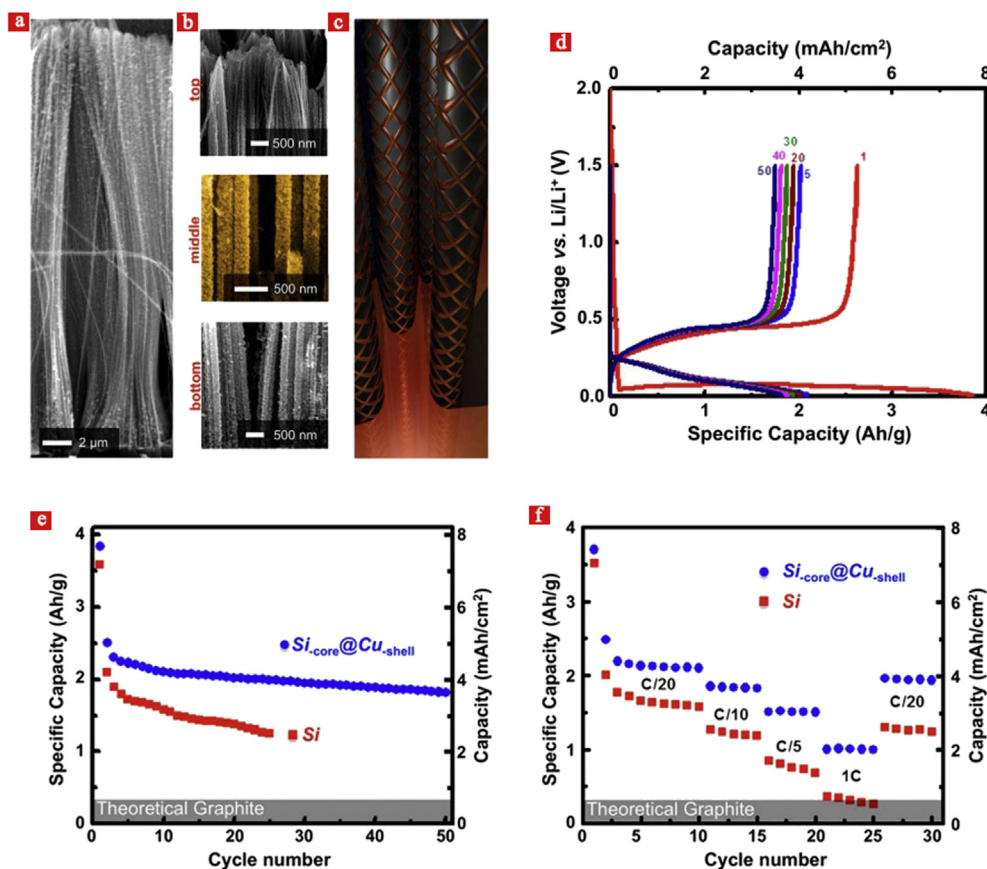


**Fig. 19.** (a) Conformal Cu coating of high aspect ratio Si nanowires with coaxial morphology through an electroless deposition protocol; (b) snapshots at different height positions evidencing the uniform Cu coating along the Si nanowires; (c) schematic representation of the Cu-wrapped Si nanowires. The Cu shell has a porous, electrically interconnected structure to allow for a faster Li<sup>+</sup> insertion, volume expansion accommodation and efficient current collection; (d) discharge/charge profiles for the Si-core@Cu-shell composite anodes cycled between 1.5 and 0.02 V; (e) capacity retention at a cycling rate of C/20 of the Si and Si-core@Cu-shell polymer electrolyte composite anodes. The theoretical capacity of graphite is highlighted for comparison [187].

capacity retention and rate capabilities as compared to pristine nanowires when integrated into LIPOSIL architecture. The obtained Si-core@Cu-shell nanowires displayed enhanced electrochemical performances due to improved current collection efficiency and Si encapsulation. The porous Cu was used to stabilize the electrodes over extended cycles and provided efficient current collection. The first discharge capacity of  $3900 \text{ mAh g}^{-1}$  was higher than that of pristine Si nanowires and the composite could sustain a capacity of  $2000 \text{ mAh g}^{-1}$  over extended cycling with little capacity decay. The Cu coating rules out the conductivity limitations and enables lithiation of the entire Si mass not only at the first discharge, but also during the subsequent cycling.

Anode performances of  $\text{LaSi}_2/\text{Si}$  composites were studied in ionic liquid electrolytes [188]. The  $\text{LaSi}_2/\text{Si}$  electrode exhibited much better performance, with reversible capacity at 250th cycle and its retention were  $800 \text{ mAh g}^{-1}$  and 80%. This performance is attributed to a higher stability of cations in the ionic liquid and an easier desolvation of Li ions and the anions. Kohandehghan et al. synthesized magnesium (Mg)- and magnesium silicide ( $\text{Mg}_2\text{Si}$ )-coated SiNWs for Li-ion batteries [189]. Both Mg- and  $\text{Mg}_2\text{Si}$ -coated materials showed significant improvement in coulombic efficiency. The large void space between the nanowire assembly and the substrate produced during cycling makes nanowires lose electrical contact with the substrate, which has been accepted as a main degradation mechanism of electrodes. An overview of the characteristics of various Si/metal based electrode materials is given in Table 3.

## 6. Understanding of the performance improvement in silicon-based composites

Study of the internal stress/strain distribution and materials failure mechanisms in nano-Si has motivated intense research. The methodologies adopted for reducing the capacity loss in Si anodes and the challenges that remain in using Si-based anodes have been

illustrated in the last few sections. A comprehensive understanding of the (de)lithiation mechanisms is among the key issues in designing and fabricating high-performance Si anodes [190,191]. Impressive results have been obtained by using in-situ Transmission Electron Microscopy (TEM) and first-principles simulation.

### 6.1. In-situ TEM

Understanding the microscopic mechanisms of electrochemical reaction and material degradation is crucial for the design of high-performance Si anodes for lithium ion batteries (LIBs). A novel nanobattery assembly and testing platform inside a TEM has been designed, which allows a direct study of the structural evolution of individual nanowire or nanoparticle electrodes with near-atomic resolution in real time. The in-situ TEM technique allows for better understanding of volume changes in SiNWs electrodes [192]. Very recently, Huang et al. developed a nanoscale open cell electrochemical device [193], allowing real-time observation of the charging/discharging behavior of individual SiNW electrodes. They demonstrated ultrafast and full electrochemical lithiation of individual carbon coated SiNWs by direct real-time observation using in-situ TEM in ionic liquid electrolytes (Fig. 20). The SiNWs didn't fracture despite the ultrahigh lithiation rates and ~300% volume expansion. Such anisotropic expansion was consistent with Cui's finding [194], and was attributed to the interfacial processes of accommodating large volumetric strains at the lithiation reaction front that depend sensitively on the crystallographic orientation. The same group studied the morphological changes in SiNWs after electrochemical cycling, and observed interesting stepwise surface roughening and nanopore evolution [195]. The study also helped explain capacity loss in Si anodes in general. In another work, the effect of metallic coatings on Si expansion was studied [55].

McDowell et al. studied the lithiation kinetics in c-SiNPs with different initial diameters using in-situ TEM [196]. They measured the

**Table 3**  
Electrochemical performance of Si/metal anodes for lithium-ion batteries.

Anode	Specific capacity ( $\text{mAh g}^{-1}$ )	Cycling stability	Synthesis methods	Reference
Si/Ge	1544.6	Capacity retention 85% after 50 cycles and doubled capacity at 3 C rate	Template-assisted synthesis method based on chemical vapor deposition process	[29]
Si/Ni	1700–2200	1500 $\text{mAh g}^{-1}$ after 700 cycles at 2 C rate	Vacuum evaporation method	[64]
Multi-layered Si/Ge	1981	Retention rate (49.3%)100 cycles	Magnetron sputtering	[161]
$\text{Si}_{0.41}\text{Ge}_{0.34}\text{Mo}_{0.25}$	1193	~870 $\text{mAh g}^{-1}$ over 100 cycles	Magnetron sputtering method	[162]
$\text{Cu-Si}_{0.6}\text{Ge}_{0.4}$	3954	1506 $\text{mAh g}^{-1}$ after 75 cycles, with the retention of 76.9%	Sputtered $\text{Si}_{(1-x)}\text{Ge}_x$ onto copper nanowires	[164]
Si/ $\text{TiSi}_2$ nanonets	1990	937 $\text{mAh g}^{-1}$ at the 100th cycle, >99% capacity retention per cycle over 100 cycles	Chemical vapor deposition	[170]
Si/ $\text{Ti}_x\text{Si}_y$	1470	1430 $\text{mAh g}^{-1}$ at 90 cycles, capacity retention 87.8% at 20 C	Silicothermic reduction	[172]
Si/Ni	3568	2660 $\text{mAh g}^{-1}$ after 100 cycles, ~85% capacity remaining after 100 cycles at 0.3 C	Chemical vapor deposition	[175]
Ni/Si	1130	580 $\text{mAh g}^{-1}$ at the 1000th cycle	Electroless deposition followed by gas deposition	[174]
$\text{Ni}_3\text{P/Si}$	1590	790 $\text{mAh g}^{-1}$ at the 1000th cycle	Electroless deposition followed by gas deposition	[174]
SiNW/TMV1cys/Ni	2300	1200 $\text{mAh g}^{-1}$ after 173 cycles, 0.25% capacity decreased per cycle	Electrodeposition on a virus-structured current collector	[178]
SiNW/Cu	3900	2000 $\text{mAh g}^{-1}$ over extended cycling with little capacity decay	Roll up nanowire battery from silicon chips	[187]
$\text{TiO}_2/\text{Si}$	2000	710 $\text{mAh g}^{-1}$ at the 900th cycle, 1870 $\text{mAh g}^{-1}$ at a current rate of 4.8 C	Sol-gel method	[168]
$\text{LaSi}_2/\text{Si}$	3300 $\text{mAh g}^{-1}$	800 $\text{mAh g}^{-1}$ at 250th cycle, 80% retention.	Mechanical alloying method	[188]



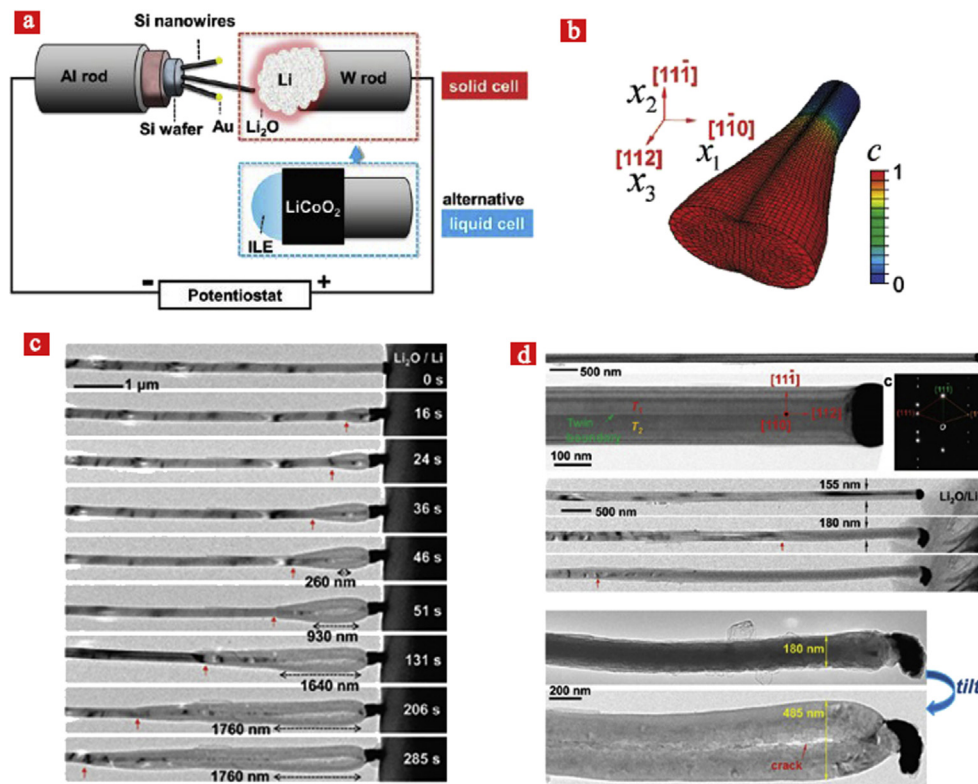


**Fig. 20.** (a) Schematic illustration of the electrochemical device; (b) simulated Li and stress distributions in a  $[111]$ -oriented Si nanowire; (c) morphology evolution of the Si nanowire during lithiation in the solid cell; (d) anisotropic swelling and crack formation of Si nanowire during lithiation [36].

positions of the reaction front during lithiation. This work inspired another group to combine experimental and theoretical study of the lithiation kinetics in individual SiNWs, as shown in Fig. 21 [197]. The results provided the quantitative data of lithiation kinetics in SiNWs and revealed the self-limiting behavior of lithiation, which is attributed to the stress-retardation effect. The same group studied the physical and chemical transformations during the Li–Si reactions [198]. The results showed that amorphous Si has more favorable kinetics and fracture behavior when reacting with Li than does crystalline Si, making it advantageous to use in battery electrodes.

Lithiation of crystalline SiNWs leads to highly anisotropic morphologies. This has been interpreted as due to anisotropy in equilibrium interface energies, but this interpretation does not capture the dynamic, nonequilibrium nature of the lithiation process. The volume expansion during initial lithiation of c-Si is highly anisotropic [36,191,194,199] with the  $\langle 110 \rangle$  orientation growing at a much faster rate than other low-index orientations, which will cause stress concentration and fracture in certain directions. Experiments also indicated that the lithiation reaction front (RF) is atomically sharp ( $\sim 1$  nm) [36,200] and progresses linearly with time [36]. Although the lithiation behavior of Si has been understood, lithium ion transport behavior across a network of Si and carbon is still unclear. Wang and coworkers probed the lithiation behavior of SiNPs attached to and embedded in a carbon nanofiber using in-situ TEM, and found that aggregated SiNPs show contact flattening upon initial lithiation, which is characteristically analogous to the classic sintering of powder particles by a neck-growth mechanism [201].

## 6.2. First-principles simulation

Analysis of the delithiation and relithiation processes provided insights into the underlying physics of the lithiation-delithiation

process, thus providing firm conceptual foundations for future design of improved Si anodes for Li ion battery applications. First-principles calculations based on density-functional theory (DFT) is widely used in investigating the electronic structure and studying a wide range of different atomic systems, including molecules, surfaces, nano-structures and bulk materials. The mechanism of lithium insertion and the interaction between Li and Si electrode must be quantitatively understood at the atomic level by first-principles simulation.

Chevrier et al. developed the protocol to simulate the molecular dynamics of Si lithiation at room temperature while avoiding the lengthy diffusion dynamics [21,202]. However, Chan et al. tested the insertion of Li into different interstitial sites and found that in only approximately 20% of all cases, the site farthest away from existing atoms is the most energetically favorable site after relaxation [203]. Tritsarlis et al. found that both the energy barriers for diffusion and the topology of the atomic structure control the ion diffusion. They also established that not all of the diffusion pathways participate equally in mediating the flow of Li atoms in the material, even if all energy barriers were assumed to be equal [204].

Experimental studies have provided strong evidence for the formation of various stable Li–Si crystalline phases during high-temperature lithiation [36,197,205]. The equilibrium titration curves of the Li–Sn and Li–Si systems are shown superimposed in Fig. 22 [205]. It can be seen that the phase  $\text{Li}_{2.6}\text{Sn}$  is stable over a range of potential, including that at which the reaction  $\text{Li} + \text{Si} = \text{Li}_{1.71}\text{Si}$  takes place, approximately 0.338 V vs. Li. as shown in Fig. 22. Many simulations have been proposed to study the structures of these crystalline phases [206–208]. In contrast to high-temperature lithiation, room-temperature Si lithiation frequently leads to amorphous lithium silicide (a- $\text{Li}_x\text{Si}$ ), which is a particularly important phase transition and structural change [209]. Using ab initio schemes, the amorphization process and structural evolution

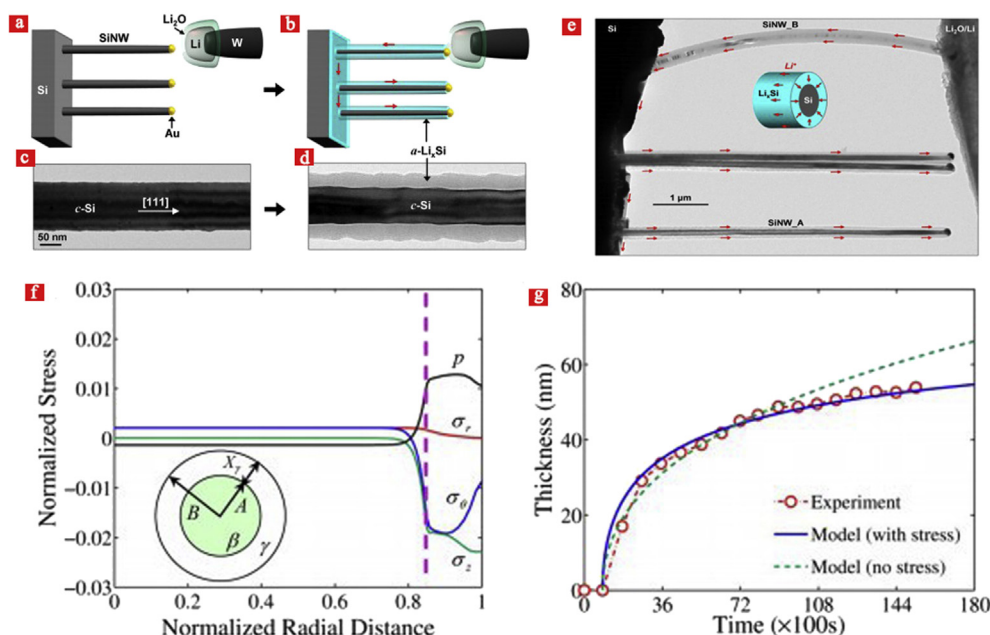


Fig. 21. In-situ lithiation of SiNWs. Modeling of stress generation and self-limiting lithiation in a SiNW [197].

of  $\text{Li}_x\text{Si}$  compounds can be studied, and many works have focused on this issue [20,210].

Using first-principles calculations, several groups investigated the characteristics of Li insertion into c-Si [203], but the reaction mechanism involving the progression of the sharp RF was not considered in these studies [211–213]. In an attempt to rationalize the experimentally observed behavior, two different groups [203,214] have recently studied the energetics of equilibrium structures at the  $\langle 110 \rangle$ ,  $\langle 111 \rangle$ , and  $\langle 100 \rangle$  interfaces between c-Si and amorphous Si (a-Si), showing that the first of these interfaces was significantly more stable than the other two. However, since lithiation of Si is a nonequilibrium process, thermodynamically stable states are not expected to form during lithiation [196,215,216]. Accordingly, arguments based on relative energies of equilibrium structures cannot capture the essence of the observed behavior; instead, kinetic rates and the dynamic evolution of the structure are crucial for understanding the lithiation process. Cubuk et al. provided a comprehensive explanation of experimentally observed morphological changes identifying reaction

paths and associated structural transformations for Li insertion into the Si  $\langle 110 \rangle$  and  $\langle 111 \rangle$  surfaces and calculated the relevant energy barriers from density functional theory methods [217]. Then they performed kinetic Monte Carlo simulations for nanowires with surfaces of different orientations, which resembled the experimentally observed profiles and the relative reaction front rates to a remarkable degree. To provide insight into the pertinent kinetic processes, Pharr et al. presented an experimental study quantifying the kinetics of the initial lithiation of crystalline Si [218]. The experiments identified the existence of a moving phase boundary for  $\langle 100 \rangle$ ,  $\langle 110 \rangle$ , and  $\langle 111 \rangle$  orientations, indicating that short range processes at the a- $\text{Li}_x\text{Si}$ /c-Si interface significantly contribute to the kinetics of the lithiation process, as shown in Fig. 23.

Besides employing DFT to examine Li incorporation in nanostructure Si [21,42,203,207,219] and graphene [220–222], the lithiation behavior of Si/graphene composites was also examined [223]. Chou et al. demonstrated charge transfer from Li to both Si and C (in graphene): the excess electrons on graphene create an electric field, which attracts Li cations while repels Si anions and thus results in a distinct alternative Li–Si layering structure near graphene. The facile interfacial Li ions diffusion contributed to high performance anodes with fast charge/discharge rates. However, the presence of graphene tends to have no significant impact on the structural evolution of Si during lithiation, as Li atoms are mostly incorporated in the Si matrix rather than at the Si/graphene interface.

Nuclear Magnetic Resonance (NMR) and Auger Electron Spectroscopy (AES) have also been used successfully to observe different Li environments in Si [142,224–226] at many stages of the (de) lithiation process.

## 7. Summary and perspective

This review has illustrated Si-based anodes in lithium batteries. Si-based anodes have considerable potential for improvement in charge capacity, coulombic efficiency and capacity retention over conventional graphite-based anodes. However, significant challenges need to be overcome before Si anodes can be utilized in practical lithium batteries. The challenges include the control of Si-

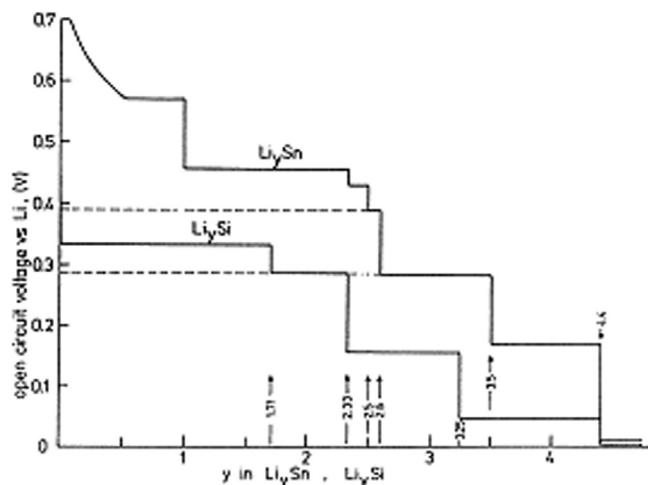
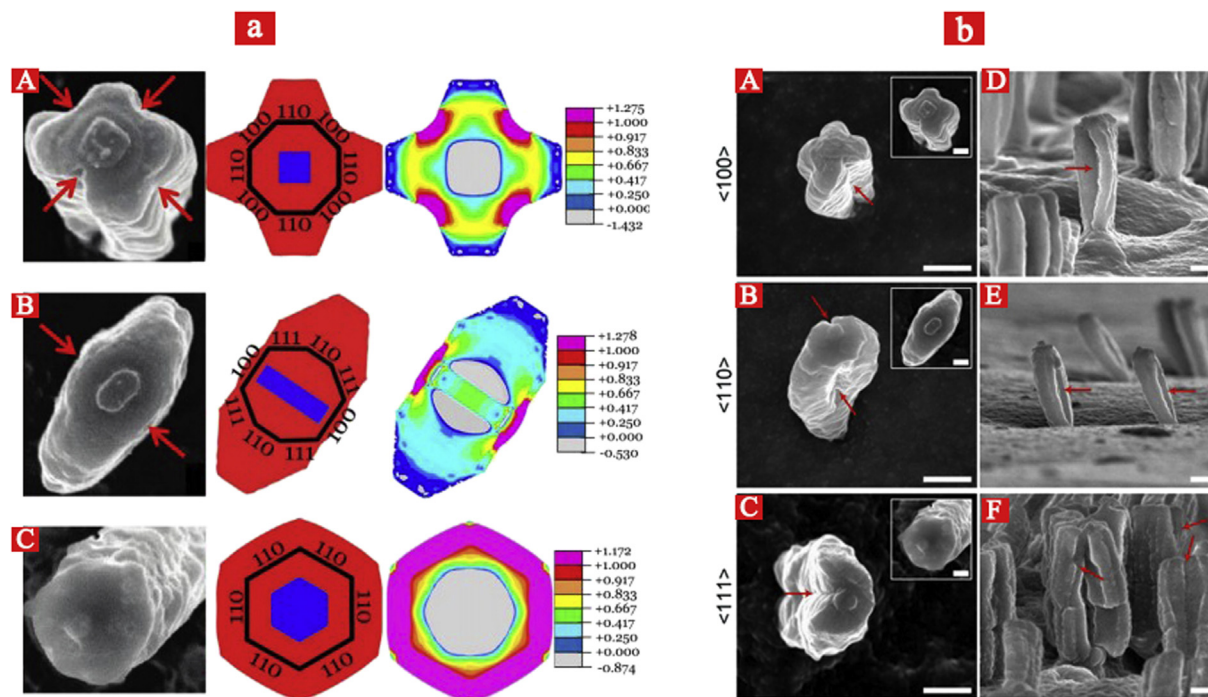


Fig. 22. Equilibrium titration curves of the Li–Sn and Li–Si systems at 415 °C [205].



**Fig. 23.** (a) Comparison between experiments and finite element simulation of lithiation of crystalline Si nanopillars of various axial orientations: A<100>, B<110>, and C<111> [226]; (b) anisotropic lateral expansion and fracture of crystalline Si nanopillars with three different axial orientations (100, 110, and 111) after lithiation [199].

based electrodes that exist and operate in a state far away from equilibrium, particularly in charged state, and the accommodation of large volumetric and/or structural changes over many charge/discharge cycles. Nanoscale morphologies have the potential to achieve long cycling lifetimes and good reversibility if stress management and stable passivation layer formation during cycling can be properly addressed.

Using conductive polymer elastomer for build-up of a coated Si anode could assure the long term stability of the anode. In addition, exterior shell can allow free expansion of the anode while retains electrical contact and serves as a barrier from further electrolyte decomposition. Carbon/alloy-Si composites have also shown immense promise. Carbon/alloy can provide a stable SEI and accommodate the stress resulted from the Si volume expansions, while Si can ensure the high capacity due to larger lithium uptake. One dimensional nanostructured materials such as NTs and NWs exhibit a significant improvement of electrochemical performance due to the short diffusion lengths and better accommodation of large volume changes.

Further research is needed to improve high-rate performance in order to make these batteries feasible for high power applications. Finally, researchers will need to look for ways to extend the cycle life of the electrodes since longevity will be a prime requirement for lithium-ion batteries to enter the commercial market.

## Acknowledgments

The authors sincerely appreciate the financial support given by the National Natural Science Foundation of China (50803008), Natural Science Foundation of Hunan (11B001, 14JJ4035), Key Laboratory for Power Technology of Renewable Energy Sources (2011KFJJ006), the State Key Laboratory of Luminescent Materials and Devices at South China University of Technology (2013-skllmd-08), China Postdoctoral Science Foundation (20100480946, 201104508).

## References

- [1] C.K. Chan, H. Peng, G. Liu, K. McIlwrath, X.F. Zhang, R.A. Huggins, Y. Cui, *Nat. Nanotechnol.* 3 (2007) 31.
- [2] R. Teki, M.K. Datta, R. Krishnan, T.C. Parker, T.M. Lu, P.N. Kumta, N. Koratkar, *Small* 5 (2009) 2236.
- [3] J.R. Szczech, S. Jin, *Energy Environ. Sci.* 4 (2011) 56.
- [4] B. Boukamp, G. Lesh, R. Huggins, *J. Electrochem. Soc.* 128 (1981) 725.
- [5] W.-J. Zhang, *J. Power Sources* 196 (2011) 13.
- [6] X.-L. Wu, Y.-G. Guo, L.-J. Wan, *Chem.—Asian J.* 8 (2013) 1948.
- [7] G.K. Simon, T. Goswami, *Metall. Mater. Trans. A* 42 (2011) 231.
- [8] S.K. Soni, B.W. Sheldon, X. Xiao, M.W. Verbrugge, D. Ahn, H. Haftbaradaran, H. Gao, *J. Electrochem. Soc.* 159 (2012) A38.
- [9] D.M. Piper, T.A. Yersak, S.H. Lee, *J. Electrochem. Soc.* 160 (2013) A77.
- [10] J. Christensen, J. Newman, *J. Solid State Electrochem.* 10 (2006) 293.
- [11] J. Christensen, J. Newman, *J. Electrochem. Soc.* 153 (2006) A1019.
- [12] X. Zhang, A.M. Sastry, W. Shyy, *J. Electrochem. Soc.* 155 (2008) A542.
- [13] Y.-T. Cheng, M.W. Verbrugge, *J. Appl. Phys.* 104 (2008) 083521.
- [14] Y.-T. Cheng, M.W. Verbrugge, *J. Power Sources* 190 (2009) 453.
- [15] R. Deshpande, Y.-T. Cheng, M.W. Verbrugge, *J. Power Sources* 195 (2010) 5081.
- [16] S. Golmon, K. Maute, S.-H. Lee, M.L. Dunn, *Appl. Phys. Lett.* 97 (2010) 033111.
- [17] T.K. Bhandakkar, H. Gao, *Int. J. Solids Struct.* 48 (2011) 2304.
- [18] W.H. Woodford, Y.-M. Chiang, W.C. Carter, *J. Electrochem. Soc.* 157 (2010) A1052.
- [19] Y. Hu, X. Zhao, Z. Suo, *J. Mater. Res.* 25 (2010) 1007.
- [20] H. Kim, C.-Y. Chou, J.G. Ekerdt, G.S. Hwang, *J. Phys. Chem. C* 115 (2011) 2514.
- [21] V.L. Chevrier, J.R. Dahn, *J. Electrochem. Soc.* 156 (2009) A454.
- [22] C.-Y. Chou, H. Kim, G.S. Hwang, *J. Phys. Chem. C* 115 (2011) 20018.
- [23] K. Zhao, W.L. Wang, J. Gregoire, M. Pharr, Z. Suo, J.J. Vlassak, E. Kaxiras, *Nano Lett.* 11 (2011) 2962.
- [24] V.A. Sethuraman, M.J. Chon, M. Shimshak, V. Srinivasan, P.R. Guduru, *J. Power Sources* 195 (2010) 5062.
- [25] P. Verma, P. Maire, P. Novák, *Electrochim. Acta* 55 (2010) 6332.
- [26] R. Ruffo, S.S. Hong, C.K. Chan, R.A. Huggins, Y. Cui, *J. Phys. Chem. C* 113 (2009) 11390.
- [27] X. Wu, Z. Wang, L. Chen, X. Huang, *Electrochem. Commun.* 5 (2003) 935.
- [28] A.A. Arie, W. Chang, J.K. Lee, *J. Electroceram.* 24 (2010) 308.
- [29] T. Song, H. Cheng, H. Choi, J.-H. Lee, H. Han, D.H. Lee, D.S. Yoo, M.-S. Kwon, J.-M. Choi, S.G. Doo, *ACS Nano* 6 (2012) 303.
- [30] T. Song, J. Xia, J.-H. Lee, D.H. Lee, M.-S. Kwon, J.-M. Choi, J. Wu, S.K. Doo, H. Chang, W.I. Park, *Nano Lett.* 10 (2010) 1710.
- [31] M.-H. Park, M.G. Kim, J. Joo, K. Kim, J. Kim, S. Ahn, Y. Cui, J. Cho, *Nano Lett.* 9 (2009) 3844.
- [32] K. Evanoff, J. Benson, M. Schauer, I. Kovalenko, D. Lashmore, W.J. Ready, G. Yushin, *ACS Nano* 6 (2012) 9837.



- [33] Z. Wen, G. Lu, S. Mao, H. Kim, S. Cui, K. Yu, X. Huang, P.T. Hurley, O. Mao, J. Chen, *Electrochem. Commun.* (2013) 67.
- [34] A. Wilson, J. Dahn, *J. Electrochem. Soc.* 142 (1995) 326.
- [35] L.-F. Cui, R. Ruffo, C.K. Chan, H. Peng, Y. Cui, *Nano Lett.* 9 (2008) 491.
- [36] X.H. Liu, H. Zheng, L. Zhong, S. Huang, K. Karki, L.Q. Zhang, Y. Liu, A. Kushima, W.T. Liang, J.W. Wang, J.H. Cho, E. Epstein, S.A. Dayeh, S.T. Picraux, T. Zhu, J. Li, J.P. Sullivan, J. Cummings, C. Wang, S.X. Mao, Z.Z. Ye, S. Zhang, J.Y. Huang, *Nano Lett.* 11 (2011) 3312.
- [37] K. Peng, J. Jie, W. Zhang, S.-T. Lee, *Appl. Phys. Lett.* 93 (2008) 033105.
- [38] R. Huang, X. Fan, W. Shen, J. Zhu, *Appl. Phys. Lett.* 95 (2009) 133119.
- [39] E. Quiroga-González, J. Carstensen, H. Föll, *Materials* 6 (2013) 626.
- [40] C.K. Chan, R. Ruffo, S.S. Hong, Y. Cui, *J. Power Sources* 189 (2009) 1132.
- [41] X.H. Liu, L.Q. Zhang, L. Zhong, Y. Liu, H. Zheng, J.W. Wang, J.H. Cho, S.A. Dayeh, S.T. Picraux, J.P. Sullivan, S.X. Mao, Z.Z. Ye, J.Y. Huang, *Nano Lett.* 11 (2011) 2251.
- [42] Q. Zhang, W. Zhang, W. Wan, Y. Cui, E. Wang, *Nano Lett.* 10 (2010) 3243.
- [43] K. Kang, H.-S. Lee, D.-W. Han, G.-S. Kim, D. Lee, G. Lee, Y.-M. Kang, M.-H. Jo, *Appl. Phys. Lett.* 96 (2010) 053110.
- [44] R. Huang, J. Zhu, *Mater. Chem. Phys.* 121 (2010) 519.
- [45] X.-L. Wang, W.-Q. Han, *ACS Appl. Mater. Interfaces* 2 (2010) 3709.
- [46] W. Xu, J.C. Flake, *J. Electrochem. Soc.* 157 (2010) A41.
- [47] N. Liu, L. Hu, M.T. McDowell, A. Jackson, Y. Cui, *ACS Nano* 5 (2011) 6487.
- [48] A.M. Chockla, J.T. Harris, V.A. Akhavan, T.D. Bogart, V.C. Holmberg, C. Steinhagen, C.B. Mullins, K.J. Stevenson, B.A. Korgel, *J. Am. Chem. Soc.* 133 (2011) 20914.
- [49] M. Ge, J. Rong, X. Fang, C. Zhou, *Nano Lett.* 12 (2012) 2318.
- [50] L. Hu, H. Wu, S.S. Hong, L. Cui, J.R. McDonough, S. Bohy, Y. Cui, *Chem. Commun.* 47 (2011) 367.
- [51] H.T. Nguyen, F. Yao, M.R. Zamfir, C. Biswas, K.P. So, Y.H. Lee, S.M. Kim, S.N. Cha, J.M. Kim, D. Pribat, *Adv. Energy Mater.* 1 (2011) 1154.
- [52] M.T. McDowell, S.W. Lee, I. Ryu, H. Wu, W.D. Nix, J.W. Choi, Y. Cui, *Nano Lett.* 11 (2011) 4018.
- [53] M.T. McDowell, Y. Cui, *Adv. Energy Mater.* 1 (2011) 894.
- [54] Q. Zhang, Y. Cui, E. Wang, *J. Phys. Chem. C* 115 (2011) 9376.
- [55] M.T. McDowell, S. Woo Lee, C. Wang, Y. Cui, *Nano Energy* 1 (2012) 401.
- [56] Y. Xiao, D. Hao, H. Chen, Z. Gong, Y. Yang, *ACS Appl. Mater. Interfaces* (2013) 1681.
- [57] E. Mullane, T. Kennedy, H. Geaney, C. Dickinson, K.M. Ryan, *Chem. Mater.* 25 (2013) 1816.
- [58] V. Chakrapani, F. Rusli, M.A. Filler, P.A. Kohl, *J. Power Sources* 205 (2012) 433.
- [59] K.-L. Lee, J.-Y. Jung, S.-W. Lee, H.-S. Moon, J.-W. Park, *J. Power Sources* 129 (2004) 270.
- [60] L. Chen, J. Xie, H. Yu, T. Wang, *J. Appl. Electrochem.* 39 (2009) 1157.
- [61] T.D. Hatchard, M.N. Obrovac, J.R. Dahna, *J. Electrochem. Soc.* 153 (2006) A282.
- [62] T. Takamura, S. Ohara, M. Uehara, J. Suzuki, K. Sekine, *J. Power Sources* 129 (2004) 96.
- [63] J. Graetz, C. Ahn, R. Yazami, B. Fultz, *Electrochem. Solid-State Lett.* 6 (2003) A194.
- [64] S. Ohara, J. Suzuki, K. Sekine, T. Takamura, *J. Power Sources* 119 (2003) 591.
- [65] J.-B. Kim, H.-Y. Lee, K.-S. Lee, S.-H. Lim, S.-M. Lee, *Electrochem. Commun.* 5 (2003) 544.
- [66] T. Moon, C. Kim, B. Park, *J. Power Sources* 155 (2006) 391.
- [67] T. Takamura, M. Uehara, J. Suzuki, K. Sekine, K. Tamura, *J. Power Sources* 158 (2006) 1401.
- [68] S. Ohara, J. Suzuki, K. Sekine, T. Takamura, *J. Power Sources* 136 (2004) 303.
- [69] M. Yoshio, T. Tsumura, N. Dimov, *J. Power Sources* 146 (2005) 10.
- [70] S.-W. Song, K.A. Striebel, R.P. Reade, G.A. Roberts, E.J. Cairns, *J. Electrochem. Soc.* 150 (2003) A121.
- [71] M. Saito, T. Yamada, C. Yodoya, A. Kamei, M. Hirota, T. Takenaka, A. Tasaka, M. Inaba, *Solid State Ionics* 225 (2012) 506.
- [72] M. Park, G. Wang, H. Liu, S. Dou, *Electrochim. Acta* 51 (2006) 5246.
- [73] Paul R. Abel, Yong-Mao Lin, Hugo Celio, Adam Heller, C.B. Mullins, *ACS Nano* 6 (2012) 2506.
- [74] L. Baggetto, R.A. Niessen, P.H. Notten, *Electrochim. Acta* 54 (2009) 5937.
- [75] X. Xiao, P. Liu, M. Verbrugge, H. Haftbaradaran, H. Gao, *J. Power Sources* 196 (2011) 1409.
- [76] L. Baggetto, D. Danilov, P.H. Notten, *Adv. Mater.* 23 (2011) 1563.
- [77] Y. He, X. Yu, Y. Wang, H. Li, X. Huang, *Adv. Mater.* 23 (2011) 4938.
- [78] J. Yang, M. Winter, J. Besenhard, *Solid State Ionics* 90 (1996) 281.
- [79] Y.-C. Yen, S.-C. Chao, H.-C. Wu, N.-L. Wu, *J. Electrochem. Soc.* 156 (2009) A95.
- [80] J. Shu, H. Li, R. Yang, Y. Shi, X. Huang, *Electrochem. Commun.* 8 (2006) 51.
- [81] M. Winter, W.K. Appel, B. Evers, T. Hodal, K.-C. Möller, I. Schneider, M. Wachtler, M.R. Wagner, G.H. Wroldnigg, J.O. Besenhard, *Monatsh. Chem./Chem. Mon.* 132 (2001) 473.
- [82] M.K. Datta, P.N. Kumta, *J. Power Sources* 158 (2006) 557.
- [83] M.K. Datta, P.N. Kumta, *J. Power Sources* 165 (2007) 368.
- [84] W.-R. Liu, J.-H. Wang, H.-C. Wu, D.-T. Shieh, M.-H. Yang, N.-L. Wu, *J. Electrochem. Soc.* 152 (2005) A1719.
- [85] S.H. Ng, J. Wang, D. Wexler, K. Konstantinov, Z.P. Guo, H.K. Liu, *Angew. Chem. Int. Ed.* 45 (2006) 6896.
- [86] H. Li, X. Huang, L. Chen, G. Zhou, Z. Zhang, D. Yu, Y. Jun Mo, N. Pei, *Solid State Ionics* 135 (2000) 181.
- [87] H. Kim, M. Seo, M.H. Park, J. Cho, *Angew. Chem. Int. Ed.* 49 (2010) 2146.
- [88] Y. Kwon, G.-S. Park, J. Cho, *Electrochim. Acta* 52 (2007) 4663.
- [89] A. Magasinski, P. Dixon, B. Hertzberg, A. Kvit, J. Ayala, G. Yushin, *Nat. Mater.* 9 (2010) 353.
- [90] A. Esmanski, G.A. Ozin, *Adv. Funct. Mater.* 19 (2009) 1999.
- [91] Y.S. Hu, R. Demir-Cakan, M.M. Titirici, J.O. Muller, R. Schlogl, M. Antonietti, J. Maier, *Angew. Chem. Int. Ed.* 47 (2008) 1645.
- [92] H. Kim, B. Han, J. Choo, J. Cho, *Angew. Chem. Int. Ed.* 47 (2008) 10151.
- [93] K.W. Kim, H. Park, J.G. Lee, J. Kim, Y.-U. Kim, J.H. Ryu, J.J. Kim, S.M. Oh, *Electrochim. Acta* 103 (2013) 226.
- [94] J. Deng, H. Ji, C. Yan, J. Zhang, W. Si, S. Baunack, S. Oswald, Y. Mei, O.G. Schmidt, *Angew. Chem.* 125 (2013) 2382.
- [95] S. Stankovich, D.A. Dikin, G.H. Dommett, K.M. Kohlhaas, E.J. Zimney, E.A. Stach, R.D. Piner, S.T. Nguyen, R.S. Ruoff, *Nature* 442 (2006) 282.
- [96] S. Zhu, C. Zhu, J. Ma, Q. Meng, Z. Guo, Z. Yu, T. Lu, Y. Li, D. Zhang, W.M. Lau, *RSC Adv.* 3 (2013) 6141.
- [97] X. Zhu, H. Chen, Y. Wang, L. Xia, Q. Tan, H. Li, Z. Zhong, F. Su, G. Zhao, *J. Mater. Chem. A* (2013) 4483.
- [98] J.-G. Ren, Q.-H. Wu, G. Hong, W.-J. Zhang, H. Wu, K. Amine, J. Yang, S.-T. Lee, *Energy Technol.* 1 (2013) 77.
- [99] K. Li, H. Xie, J. Liu, Z. Ma, Y. Zhou, D. Xue, *Phys. Chem. Chem. Phys.* 15 (2013) 17658.
- [100] Y. Wen, Y. Zhu, A. Langrock, A. Manivannan, S.H. Ehrman, C. Wang, *Small* 9 (2013) 2810.
- [101] J.K. Lee, K.B. Smith, C.M. Hayner, H.H. Kung, *Chem. Commun.* 46 (2010) 2025.
- [102] J. Luo, X. Zhao, J. Wu, H.D. Jang, H.H. Kung, J. Huang, *J. Phys. Chem. Lett.* 3 (2012) 1824.
- [103] Y. Sun, Q. Wu, G. Shi, *Energy Environ. Sci.* 4 (2011) 1113.
- [104] Y. Zhu, W. Liu, X. Zhang, J. He, J. Chen, Y. Wang, T. Cao, *Langmuir: ACS J. Surf. Colloids* 29 (2013) 744.
- [105] B. Wang, X. Li, X. Zhang, B. Luo, M. Jin, M. Liang, S.A. Dayeh, S. Picraux, L. Zhi, *ACS Nano* (2013) 1437.
- [106] X. Zhou, Y.-X. Yin, L.-J. Wan, Y.-G. Guo, *Chem. Commun.* 48 (2012) 2198.
- [107] H. Xiang, K. Zhang, G. Ji, J.Y. Lee, C. Zou, X. Chen, J. Wu, *Carbon* 49 (2011) 1787.
- [108] R.C. de Guzman, J. Yang, M.M.-C. Cheng, S.O. Salley, K.S. Ng, *J. Mater. Sci.* 48 (2013) 4823.
- [109] A. Gohier, B. Laik, K.H. Kim, J.L. Maurice, J.P. Pereira-Ramos, C.S. Cojocar, P. Van Tran, *Adv. Mater.* 24 (2012) 2592.
- [110] Y. Li, G. Xu, L. Xue, S. Zhang, Y. Yao, Y. Lu, O. Toprakci, X. Zhang, *J. Electrochem. Soc.* 160 (2013) A528.
- [111] K. Evanoff, J. Khan, A.A. Balandin, A. Magasinski, W.J. Ready, T.F. Fuller, G. Yushin, *Adv. Mater.* 24 (2012) 533.
- [112] K.-S. Park, K.-M. Min, S.-D. Seo, G.-H. Lee, H.-W. Shim, D.-W. Kim, *Mater. Res. Bull.* 48 (2013) 1732.
- [113] J.L. Gómez-Cámer, J. Morales, L. Sánchez, *J. Mater. Chem.* 21 (2011) 811.
- [114] S.A. Klankowski, R.A. Rojas, B.A. Cruden, J. Liu, J. Wu, J. Li, *J. Mater. Chem. A* 1 (2013) 1055.
- [115] Y. Fan, Q. Zhang, C. Lu, Q. Xiao, X. Wang, B. kang Tay, *Nanoscale* 5 (2013) 1503.
- [116] L. Hu, H. Wu, Y. Gao, A. Cao, H. Li, J. McDough, X. Xie, M. Zhou, Y. Cui, *Adv. Energy Mater.* 1 (2011) 523.
- [117] S. Chen, M.L. Gordin, R. Yi, G. Howlett, H. Sohn, D. Wang, *Phys. Chem. Chem. Phys.: PCCP* 14 (2012) 12741.
- [118] Z. Guo, J. Wang, H. Liu, S. Dou, *J. Power Sources* 146 (2005) 448.
- [119] S. Chew, Z. Guo, J. Wang, J. Chen, P. Munroe, S. Ng, L. Zhao, H. Liu, *Electrochem. Commun.* 9 (2007) 941.
- [120] H.-S. La, K.-S. Park, K.-S. Nahm, K.-K. Jeong, Y.-S. Lee, *Colloids Surf. A: Physicochem. Eng. Asp.* 272 (2006) 22.
- [121] Z. Du, S. Zhang, Y. Liu, J. Zhao, R. Lin, T. Jiang, *J. Mater. Chem.* 22 (2012) 11636.
- [122] J. Yao, Z. Jia, P. Zhang, C. Shen, J. Wang, K.-F. Aguey-Zinsou, L. Wang, *Ionics* 19 (2012) 401.
- [123] X.-y. Zhou, J.-j. Tang, J. Yang, Y.-l. Zou, S.-c. Wang, J. Xie, L.-l. Ma, *Electrochim. Acta* (2012) 296.
- [124] J.-J. Cai, P.-J. Zuo, X.-Q. Cheng, Y.-H. Xu, G.-P. Yin, *Electrochem. Commun.* 12 (2010) 1572.
- [125] Q. Liu, M.H. Nayfeh, S.-T. Yau, *J. Power Sources* 195 (2010) 3956.
- [126] L. Zhan, Z. Song, J. Zhang, J. Tang, H. Zhan, Y. Zhou, C. Zhan, *Electrochim. Acta* 53 (2008) 8319.
- [127] A.V. Murugan, M. Quintin, M.-H. Delville, G. Campet, C.S. Gopinath, K. Vijayamohan, *J. Power Sources* 156 (2006) 615.
- [128] C. Arbizzi, A. Balducci, M. Mastragostino, M. Rossi, F. Soavi, *J. Electroanal. Chem.* 553 (2003) 125.
- [129] S. Ito, T. Murata, M. Hasegawa, Y. Bito, Y. Toyoguchi, *J. Power Sources* 68 (1997) 245.
- [130] Y. Wu, S. Fang, Y. Jiang, R. Holze, *J. Power Sources* 108 (2002) 245.
- [131] X. Li, Y. Cao, W. Qi, L.V. Saraf, J. Xiao, Z. Nie, J. Mietek, J.-G. Zhang, B. Schwenzer, *J. Liu, J. Mater. Chem.* 21 (2011) 16603.
- [132] Y. Yang, G. Yu, J.J. Cha, H. Wu, M. Vosguerichian, Y. Yao, Z. Bao, Y. Cui, *ACS Nano* 5 (2011) 9187.
- [133] L. Yue, S. Wang, X. Zhao, L. Zhang, *J. Mater. Chem.* 22 (2012) 1094.
- [134] L. Yue, H. Zhong, D. Tang, L. Zhang, *J. Solid State Electrochem.* (2012) 1.
- [135] Y. Yao, N. Liu, M.T. McDowell, M. Pasta, Y. Cui, *Energy Environ. Sci.* (2012) 7927.
- [136] I. Kovalenko, B. Zdyrko, A. Magasinski, B. Hertzberg, Z. Milicev, R. Burtovyy, I. Luzinov, G. Yushin, *Science* 334 (2011) 75.

- [137] L.-F. Cui, L. Hu, H. Wu, J.W. Choi, Y. Cui, *J. Electrochem. Soc.* 158 (2011) A592.
- [138] R.R. Garsuch, D.-B. Le, A. Garsuch, J. Li, S. Wang, A. Farooq, J. Dahn, *J. Electrochem. Soc.* 155 (2008) A721.
- [139] S. Komaba, N. Yabuuchi, T. Ozeki, Z.-J. Han, K. Shimomura, H. Yui, Y. Katayama, T. Miura, *J. Phys. Chem. C* 116 (2011) 1380.
- [140] J. Li, L. Christensen, M. Obrovac, K. Hewitt, J. Dahn, *J. Electrochem. Soc.* 155 (2008) A234.
- [141] J.-S. Bridel, T. Azais, M. Morcrette, J.-M. Tarascon, D. Larcher, *Chem. Mater.* 22 (2009) 1229.
- [142] B. Key, R. Bhattacharyya, M. Morcrette, V. Seznec, J.-M. Tarascon, C.P. Grey, *J. Am. Chem. Soc.* 131 (2009) 9239.
- [143] B. Lestriez, S. Bahri, I. Sandu, L. Roué, D. Guyomard, *Electrochem. Commun.* 9 (2007) 2801.
- [144] N. Hochgatterer, M. Schweiger, S. Koller, P. Raimann, T. Wöhrle, C. Wurm, M. Winter, *Electrochem. Solid-State Lett.* 11 (2008) A76.
- [145] J. Guo, C. Wang, *Chem. Commun.* 46 (2010) 1428.
- [146] A. Magasinski, B. Zdyrko, I. Kovalenko, B. Hertzberg, R. Burtovyy, C.F. Huebner, T.F. Fuller, I. Luzinov, G. Yushin, *ACS Appl. Mater. Interfaces* 2 (2010) 3004.
- [147] Z.-J. Han, N. Yabuuchi, K. Shimomura, M. Murase, H. Yui, S. Komaba, *Energy Environ. Sci.* 5 (2012) 9014.
- [148] S. Komaba, T. Ozeki, N. Yabuuchi, K. Shimomura, *Electrochemistry* 79 (2011) 6.
- [149] S. Komaba, K. Okushi, T. Ozeki, H. Yui, Y. Katayama, T. Miura, T. Saito, H. Kroult, *Electrochem. Solid-State Lett.* 12 (2009) A107.
- [150] N. Yabuuchi, K. Shimomura, Y. Shimbe, T. Ozeki, J.Y. Son, H. Oji, Y. Katayama, T. Miura, S. Komaba, *Adv. Energy Mater.* 1 (2011) 759.
- [151] Y. Wei, H. Yu, H. Li, H. Ming, K. Pan, H. Huang, Y. Liu, Z. Kang, *Mater. Res. Bull.* 48 (2013) 4072.
- [152] M. Murase, N. Yabuuchi, Z.J. Han, J.Y. Son, Y.T. Cui, H. Oji, S. Komaba, *ChemSusChem* 5 (2012) 2307.
- [153] M.H. Ryou, J. Kim, I. Lee, S. Kim, Y.K. Jeong, S. Hong, J.H. Ryu, T.S. Kim, J.K. Park, H. Lee, J.W. Choi, *Adv. Mater.* 25 (2013) 1571.
- [154] G. Liu, S. Xun, N. Vukmirovic, X. Song, P. Olalde-Velasco, H. Zheng, V.S. Battaglia, L. Wang, W. Yang, *Adv. Mater.* 23 (2011) 4679.
- [155] M. Wu, X. Xiao, N. Vukmirovic, S. Xun, P.K. Das, X. Song, P. Olalde-Velasco, D. Wang, A.Z. Weber, L.-W. Wang, *J. Am. Chem. Soc.* 135 (2013) 12048.
- [156] A.M. Chockla, K. Klavetter, C.B. Mullins, B.A. Korgel, *ACS Appl. Mater. Interfaces* (2012) 4658.
- [157] M.-H. Seo, M. Park, K.T. Lee, K. Kim, J. Kim, J. Cho, *Energy Environ. Sci.* 4 (2011) 425.
- [158] A.M. Chockla, M.G. Panthani, V.C. Holmberg, C.M. Hessel, D.K. Reid, T.D. Bogart, J.T. Harris, C.B. Mullins, B.A. Korgel, *J. Phys. Chem. C* 116 (2012) 11917.
- [159] C.K. Chan, X.F. Zhang, Y. Cui, *Nano Lett.* 8 (2008) 307.
- [160] F.-W. Yuan, H.-J. Yang, H.-Y. Tuan, *ACS Nano* 6 (2012) 9932.
- [161] C.-M. Hwang, C.-H. Lim, J.-W. Park, *Thin Solid Films* (2010) 2332.
- [162] C.-M. Hwang, J.-W. Park, *Electrochim. Acta* 56 (2011) 6737.
- [163] Y. Hashimoto, N. Machida, T. Shigematsu, *Solid State Ionics* 175 (2004) 177.
- [164] J. Wang, N. Du, H. Zhang, J. Yu, D. Yang, *J. Power Sources* 208 (2012) 434.
- [165] P.R. Abel, A.M. Chockla, Y.-M. Lin, V.C. Holmberg, J.T. Harris, B.A. Korgel, A. Heller, C.B. Mullins, *ACS Nano* (2013) 2249.
- [166] W. Liang, H. Yang, F. Fan, Y. Liu, X.-H. Liu, J.Y. Huang, T. Zhu, S. Zhang, *ACS Nano* 7 (2013) 3427.
- [167] H. Geaney, E. Mullane, Q.M. Ramasse, K.M. Ryan, *Nano Lett.* 13 (2013) 1675.
- [168] H. Usui, K. Wasada, M. Shimizu, H. Sakaguchi, *Electrochim. Acta* 111 (2013) 575.
- [169] I.S. Kim, P. Kumta, G. Blomgren, *Electrochem. Solid-State Lett.* 3 (2000) 493.
- [170] S. Zhou, X. Liu, D. Wang, *Nano Lett.* 10 (2010) 860.
- [171] H.-G. Jung, S.W. Oh, J. Ce, N. Jayaprakash, Y.-K. Sun, *Electrochem. Commun.* 11 (2009) 756.
- [172] O. Park, J.-I. Lee, M.-J. Chun, J.-T. Yeon, S. Yoo, S. Choi, N.-S. Choi, S. Park, *RSC Adv.* 3 (2013) 2538.
- [173] C. Loka, H. Yu, K.-S. Lee, J. Cho, *J. Power Sources* 244 (2013) 259.
- [174] H. Usui, M. Shibata, K. Nakai, H. Sakaguchi, *J. Power Sources* 196 (2011) 2143.
- [175] H. Zhang, P.V. Braun, *Nano Lett.* 12 (2012) 2778.
- [176] K.T. Nam, D.W. Kim, P.J. Yoo, C.Y. Chiang, N. Meethong, P.T. Hammond, Y.M. Chiang, A.M. Belcher, *Science* 312 (2006) 885.
- [177] Y.J. Lee, H. Yi, W.-J. Kim, K. Kang, D.S. Yun, M.S. Strano, G. Ceder, A.M. Belcher, *Science* 324 (2009) 1051.
- [178] X. Chen, K. Gerasopoulos, J. Guo, A. Brown, C. Wang, R. Ghodssi, J.N. Culver, *Adv. Funct. Mater.* 21 (2011) 380.
- [179] E. Royston, A. Ghosh, P. Kofinas, M.T. Harris, J.N. Culver, *Langmuir: ACS J. Surf. Colloids* 24 (2008) 906.
- [180] X. Chen, K. Gerasopoulos, J. Guo, A. Brown, C. Wang, R. Ghodssi, J.N. Culver, *ACS Nano* 4 (2010) 5366.
- [181] K. Gerasopoulos, M. McCarthy, P. Banerjee, X. Fan, J. Culver, R. Ghodssi, *Nanotechnology* 21 (2010) 055304.
- [182] D.C. Johnson, J.M. Mosby, S.C. Riha, A.L. Prieto, J. Mater. Chem. 20 (2010) 1993.
- [183] V.A. Sethuraman, K. Kowolik, V. Srinivasan, *J. Power Sources* 196 (2011) 393.
- [184] H. Chen, Y. Xiao, L. Wang, Y. Yang, *J. Power Sources* 196 (2011) 6657.
- [185] C. Joyce, L. Trahey, S.A. Bauer, F. Dogan, J.T. Vaughney, *J. Electrochem. Soc.* 159 (2012) A909.
- [186] S. Murugesan, J.T. Harris, B.A. Korgel, K.J. Stevenson, *Chem. Mater.* 24 (2012) 1306.
- [187] A. Vlad, A.L.M. Reddy, A. Ajayan, N. Singh, J.-F. Gohy, S. Melinte, P.M. Ajayan, *Proc. Natl. Acad. Sci. U. S. A.* 109 (2012) 15168.
- [188] H. Usui, M. Shimizu, H. Sakaguchi, *J. Power Sources* 235 (2013) 29.
- [189] A. Kohandehghan, P. Kalisvaart, M. Kupsta, B. Zahiri, B.S. Amirkhiz, Z. Li, E.L. Memarzadeh, L.A. Bendersky, D. Mitlin, *J. Mater. Chem. A* 1 (2013) 1600.
- [190] M. Ulldemolins, F.L. Cras, B. Pecquenard, *Electrochem. Commun.* 27 (2013) 22.
- [191] J.L. Goldman, B.R. Long, A.A. Gewirth, R.G. Nuzzo, *Adv. Funct. Mater.* 21 (2011) 2412.
- [192] N. Kawamoto, D.M. Tang, X. Wei, X. Wang, M. Mitome, Y. Bando, D. Golberg, *J. Electron Microscopy* 62 (2013) 157.
- [193] J.Y. Huang, L. Zhong, C.M. Wang, J.P. Sullivan, W. Xu, L.Q. Zhang, S.X. Mao, N.S. Hudak, X.H. Liu, A. Subramanian, *Science* 330 (2010) 1515.
- [194] S.W. Lee, M.T. McDowell, J.W. Choi, Y. Cui, *Nano Lett.* 11 (2011) 3034.
- [195] J.W. Choi, J. McDonough, S. Jeong, J.S. Yoo, C.K. Chan, Y. Cui, *Nano Lett.* 10 (2010) 1409.
- [196] M.T. McDowell, I. Ryu, S.W. Lee, C. Wang, W.D. Nix, Y. Cui, *Adv. Mater.* 24 (2012) 6034.
- [197] X.-H. Liu, F. Fan, H. Yang, S. Zhang, J.Y. Huang, T. Zhu, *ACS Nano* (2013) 1495.
- [198] M.T. McDowell, S.W. Lee, J.T. Harris, B.A. Korgel, C. Wang, W.D. Nix, Y. Cui, *Nano Lett.* 13 (2013) 758.
- [199] S.W. Lee, M.T. McDowell, L.A. Berla, W.D. Nix, Y. Cui, *Proc. Natl. Acad. Sci. U. S. A.* 109 (2012) 4080.
- [200] M.J. Chon, V.A. Sethuraman, A. McCormick, V. Srinivasan, P.R. Guduru, *Phys. Rev. Lett.* 107 (2011) 045503.
- [201] M. Gu, Y. Li, X. Li, S. Hu, X. Zhang, W. Xu, S. Thevuthasan, D.R. Baer, J.-G. Zhang, J. Liu, *ACS Nano* 6 (2012) 8439.
- [202] V.L. Chevrier, J.R. Dahn, *J. Electrochem. Soc.* 157 (2010) A392.
- [203] M.K. Chan, C. Wolverton, J.P. Greeley, *J. Am. Chem. Soc.* 134 (2012) 14362.
- [204] G.A. Tritsarlis, K. Zhao, O.U. Okeke, E. Kaxiras, *J. Phys. Chem. C* 116 (2012) 22212.
- [205] R.A. Huggins, *J. Power Sources* 81 (1999) 13.
- [206] Y. Kubota, M.C.S. Escano, H. Nakanishi, H. Kasai, *J. Appl. Phys.* 102 (2007) 053704.
- [207] V. Chevrier, J. Zwanziger, J. Dahn, *J. Alloys Compd.* 496 (2010) 25.
- [208] Y.H. Xu, G.P. Yin, P.J. Zuo, *Electrochim. Acta* 54 (2008) 341.
- [209] P. Limthongkul, Y.-I. Jang, N.J. Dudney, Y.-M. Chiang, *Acta Mater.* 51 (2003) 1103.
- [210] S.C. Jung, Y.-K. Han, *Electrochim. Acta* 62 (2012) 73.
- [211] P. Johari, Y. Qi, V.B. Shenoy, *Nano Lett.* 11 (2011) 5494.
- [212] H.Y. Lv, H. Jiang, H.J. Liu, J. Shi, *J. Appl. Phys.* 112 (2012) 103509.
- [213] S.C. Jung, Y.-K. Han, *Phys. Chem. Chem. Phys.* 13 (2011) 21282.
- [214] S.C. Jung, J.W. Choi, Y.-K. Han, *Nano Lett.* 12 (2012) 5342.
- [215] K. Zhao, G.A. Tritsarlis, M. Pharr, W.L. Wang, O. Okeke, Z. Suo, J.J. Vlassak, E. Kaxiras, *Nano Lett.* 12 (2012) 4397.
- [216] S.W. Lee, L.A. Berla, M.T. McDowell, W.D. Nix, Y. Cui, *Israel J. Chem.* 52 (2012) 1118.
- [217] E.D. Cubuk, W.L. Wang, K. Zhao, J.J. Vlassak, Z. Suo, E. Kaxiras, *Nano Lett.* (2013) 2011.
- [218] M. Pharr, K. Zhao, X. Wang, Z. Suo, J.J. Vlassak, *Nano Lett.* 12 (2012) 5039.
- [219] T.-L. Chan, J.R. Chelikowsky, *Nano Lett.* 10 (2010) 821.
- [220] A. Garay-Tapia, A.H. Romero, V. Barone, *J. Chem. Theory Comput.* 8 (2012) 1064.
- [221] X. Fan, W. Zheng, J.-L. Kuo, *ACS Appl. Mater. Interfaces* 4 (2012) 2432.
- [222] J. Zheng, Z. Ren, P. Guo, L. Fang, J. Fan, *Appl. Surf. Sci.* 258 (2011) 1651.
- [223] C.-Y. Chou, G.S. Hwang, *J. Phys. Chem. C* 117 (2013) 9598.
- [224] J.-H. Trill, C. Tao, M. Winter, S. Passerini, H. Eckert, *J. Solid State Electrochem.* 15 (2011) 349.
- [225] B. Key, M. Morcrette, J.-M. Tarascon, C.P. Grey, *J. Am. Chem. Soc.* 133 (2011) 503.
- [226] E. Radvanyi, E. De Vito, W. Porcher, J. Danet, P. Desbois, J.-F. Colin, S.J. Si Larbi, *J. Mater. Chem. A* 1 (2013) 4956.
- [227] M.K. Datta, J. Maranchi, S.J. Chung, R. Epur, K. Kadakia, P. Jampani, P.N. Kumta, *Electrochim. Acta* 56 (2011) 4717.
- [228] W. Wang, P.N. Kumta, *ACS Nano* 4 (2010) 2233.
- [229] W. Li, R. Yang, X. Wang, T. Wang, J. Zheng, X. Li, *J. Power Sources* 221 (2013) 242.
- [230] X. Zhou, L.J. Wan, Y.G. Guo, *Small* 9 (2013) 2684.
- [231] J. Kong, W.A. Yee, Y. Wei, L. Yang, J.M. Ang, S. Phua, S.Y. Wong, R. Zhou, Y. Dong, X. Li, *Nanoscale* (2013) 2967.
- [232] L.-F. Cui, L. Hu, J.W. Choi, Y. Cui, *ACS Nano* 4 (2010) 3671.